

SEMI-EMPIRICAL, FIRST-PRINCIPLES, AND HYBRID MODELING OF THE THERMOSPHERE TO ENHANCE DATA ASSIMILATION

Eric K. Sutton

27 October 2015

Final Report

APPROVED FOR PUBLIC RELEASE; DISTRIBUTION IS UNLIMITED.



**AIR FORCE RESEARCH LABORATORY
Space Vehicles Directorate
3550 Aberdeen Ave SE
AIR FORCE MATERIEL COMMAND
KIRTLAND AIR FORCE BASE, NM 87117-5776**

DTIC COPY

NOTICE AND SIGNATURE PAGE

Using Government drawings, specifications, or other data included in this document for any purpose other than Government procurement does not in any way obligate the U.S. Government. The fact that the Government formulated or supplied the drawings, specifications, or other data does not license the holder or any other person or corporation; or convey any rights or permission to manufacture, use, or sell any patented invention that may relate to them.

This report was cleared for public release by the PRS OPSEC Office and is available to the general public, including foreign nationals. Copies may be obtained from the Defense Technical Information Center (DTIC) (<http://www.dtic.mil>).

AFRL-RV-PS-TR-2015-0168 HAS BEEN REVIEWED AND IS APPROVED FOR PUBLICATION IN ACCORDANCE WITH ASSIGNED DISTRIBUTION STATEMENT.

//SIGNED//

Dr. Eric K. Sutton
Project Manager, AFRL/RVBXI

//SIGNED//

Glenn M. Vaughan, Colonel, USAF
Chief, Battlespace Environment Division

This report is published in the interest of scientific and technical information exchange, and its publication does not constitute the Government's approval or disapproval of its ideas or findings.

REPORT DOCUMENTATION PAGE				Form Approved OMB No. 0704-0188	
Public reporting burden for this collection of information is estimated to average 1 hour per response, including the time for reviewing instructions, searching existing data sources, gathering and maintaining the data needed, and completing and reviewing this collection of information. Send comments regarding this burden estimate or any other aspect of this collection of information, including suggestions for reducing this burden to Department of Defense, Washington Headquarters Services, Directorate for Information Operations and Reports (0704-0188), 1215 Jefferson Davis Highway, Suite 1204, Arlington, VA 22202-4302. Respondents should be aware that notwithstanding any other provision of law, no person shall be subject to any penalty for failing to comply with a collection of information if it does not display a currently valid OMB control number. PLEASE DO NOT RETURN YOUR FORM TO THE ABOVE ADDRESS.					
1. REPORT DATE (DD-MM-YYYY) 27-10-2015		2. REPORT TYPE Final Report		3. DATES COVERED (From - To) 01 Oct 2012 – 30 Sep 2015	
4. TITLE AND SUBTITLE Semi-Empirical, First-Principles, and Hybrid Modeling of the Thermosphere to Enhance Data Assimilation				5a. CONTRACT NUMBER	
				5b. GRANT NUMBER	
				5c. PROGRAM ELEMENT NUMBER 61102F	
6. AUTHOR(S) Eric K. Sutton				5d. PROJECT NUMBER 3001	
				5e. TASK NUMBER PPM00018035	
				5f. WORK UNIT NUMBER EF122000	
7. PERFORMING ORGANIZATION NAME(S) AND ADDRESS(ES) Air Force Research Laboratory Space Vehicles Directorate 3550 Aberdeen Avenue SE Kirtland AFB, NM 87117-5776				8. PERFORMING ORGANIZATION REPORT NUMBER AFRL-RV-PS-TR-2015-0168	
9. SPONSORING / MONITORING AGENCY NAME(S) AND ADDRESS(ES)				10. SPONSOR/MONITOR'S ACRONYM(S) AFRL/RVBXI	
				11. SPONSOR/MONITOR'S REPORT NUMBER(S)	
12. DISTRIBUTION / AVAILABILITY STATEMENT Approved for public release; distribution is unlimited. (OPS-15-9186 dtd 17 Nov 2015)					
13. SUPPLEMENTARY NOTES					
14. ABSTRACT During this task, we established a method for extracting the most significant basis functions from a physics-based model of the thermosphere and ionosphere. A new model was then constructed by replacing the spherical harmonic functions used in an existing semi-empirical thermosphere model with these basis functions. The resulting hybrid model, published in the Space Weather Journal, demonstrated the ability to represent sparse thermospheric data in a more accurate and efficient way. In addition, we chose Jacchia 1970 as our underlying semi-empirical model so that the new hybrid model functions as a direct replacement for the High Accuracy Satellite Drag Model used by AFSPC and the JSPOC. We also worked to improve the hybrid model by investigating the limitations of and possible improvements to the underlying assumptions imposed by the chosen models. In particular, we realized that there was a large and potentially significant component missing from all general circulation models, that being the appropriate treatment of helium in the upper thermosphere. To rectify this situation, we undertook the project of adding helium to the solution of a first-principles community model of the thermosphere and ionosphere. In doing this, we discovered that this could only be done self-consistently by solving for helium as a major species, as opposed to as a minor species. The product of this work was the first physics-based model to accurately simulate the seasonal and latitudinal behavior of the helium distribution. This work was published in the Journal of Geophysical Research.					
15. SUBJECT TERMS satellite drag, thermosphere density, HASDM, principal components, hybrid model, helium model, neutral composition, low-Earth orbit					
16. SECURITY CLASSIFICATION OF:			17. LIMITATION OF ABSTRACT Unlimited	18. NUMBER OF PAGES 64	19a. NAME OF RESPONSIBLE PERSON Dr. Eric Sutton
a. REPORT Unclassified	b. ABSTRACT Unclassified	c. THIS PAGE Unclassified			19b. TELEPHONE NUMBER (include area code)

This page is intentionally left blank.

Table of Contents

1	Introduction	1
2	Thermospheric Basis Functions	2
2.1	Background	2
2.2	Methods, Assumptions, and Procedures	2
2.2.1	The Jacchia Semi-Empirical Model	2
2.2.2	The TIE-GCM First-Principles Model	3
2.2.3	Construction of Basis Functions	4
2.3	Results and Discussion	8
2.4	Conclusions	13
3	First-Principles Helium Model	15
3.1	Background	15
3.2	Methods, Assumptions, and Procedures	17
3.2.1	The TIE-GCM Baseline Model	17
3.2.2	Implementing Helium as a Major Species	18
3.2.3	Boundary Conditions	21
3.2.4	Software Development	23
3.3	Results and Discussion	25
3.4	Conclusions	30
3.5	Additional Supporting Information	32
	REFERENCES	37
	Appendix A: In-House Activities	43
A.1	Final Laboratory Task Report	43
A.2	Invited Talks and Lectures	43
A.3	Scientific Visits	44
A.4	Publications	44
A.4.1	First-Authored	44
A.4.2	Co-Authored	44
A.5	Presentations	45
A.6	Professional Activities	47
A.7	Technology assists, transitions, or transfers	47
	Appendix B: Time-dependent Thermospheric Composition for N Components	49
B.1	Introduction and Nomenclature	49
B.2	Mass Continuity	50
B.3	Molecular and Thermal Diffusion	51
B.4	Eddy Diffusion	53
B.5	Composition Equation	54

List of Figures

1	Distribution of ensemble parameters	5
2	Temperature/density vertical profile	7
3	ΔT_c expansion functions	9
4	ΔT_x expansion functions	10
5	Cumulative fractional variance	11
6	ΔT_c reconstruction	11
7	ΔT_x reconstruction	12
8	Neutral Density reconstruction	12
9	Relative RMS error.....	13
10	Mass mixing ratio vertical profile	20
11	Helium concentration (TIE-GCM)	26
12	Helium concentration (MSIS)	28
13	Winter helium bulge ratio.....	29
14	Helium's impact on mass density	30
15	Helium's impact on geopotential height and horizontal winds	31
16	TIE-GCM control run: constant $M_{10.7}$ and K_P	33
17	TIE-GCM control run: elevated K_P	34
18	TIE-GCM control run: elevated $M_{10.7}$	35
19	TIE-GCM control run: Tidal Forcing Removed	36

List of Tables

1	Mutual diffusion coefficients for helium with major species	21
2	Software development history	23

This page is intentionally left blank.

1 Introduction

During this task, we established a method for extracting the most significant basis functions from a physics-based model of the thermosphere and ionosphere. A new model was then constructed by replacing the spherical harmonic functions used in an existing semi-empirical thermosphere model with these basis functions. The resulting hybrid model, published in the *Space Weather Journal* (*Sutton et al.* [71]), demonstrated the ability to represent sparse thermospheric data in a more accurate and efficient way. In addition, we chose Jacchia 1970 as our underlying semi-empirical model so that the new hybrid model functions as a direct replacement for the High Accuracy Satellite Drag Model [69] (HASDM) used by AFSPC and the JSPOC.

We also worked to improve the hybrid model by investigating the limitations of and possible improvements to the underlying assumptions imposed by the chosen models. In particular, we realized that there was a large and potentially significant component missing from all general circulation models, that being the appropriate treatment of helium in the upper thermosphere. While helium concentration in the lower thermosphere constitutes merely a minor constituent, its small atomic mass compared with that of N_2 , O_2 , and O causes its concentration to decrease much more slowly with altitude. At some height, helium overtakes N_2 , O_2 , and O as the dominant species. Generally this occurs between 400 and 800 km, depending on season, location, and solar flux. At this transition altitude, the scale height—which gives an indication of the exponential rate of decay of mass density with altitude—quickly transitions from ~ 50 km to ~ 200 km.

Not only is the omission of helium an issue for physical models, but the Jacchia 1970 model, JB2006, and JB2008 all suffer from this problem as well. Because these models do not correctly account for helium, their vertical structures can be grossly inaccurate in the upper thermosphere. The impact on the operational system is clearly seen from the well-known fact that HASDM quickly loses accuracy at high altitudes and high latitudes, i.e. where helium concentrations are highest. In effect, the bulk of the data used to drive HASDM comes from altitudes around 300-500 km; however, this information is being inaccurately extrapolated to higher altitudes around 700-1000 km, a region through which more than 10,000 trackable objects travel (or about 75% of all trackable LEO objects).

To rectify this situation, we undertook the project of adding helium to the solution of a popular first-principles model of the thermosphere and ionosphere. In doing this, we discovered that this could only be done self-consistently by solving for helium as a major species, as opposed to as a minor species. The product of this work was the first physics-based model to accurately simulate the seasonal and latitudinal behavior of the helium distribution. This work was published in the *Journal of Geophysical Research* (*Sutton et al.* [72]).

2 Thermospheric Basis Functions

2.1 Background

Atmospheric drag is the dominant and most difficult force to determine and predict, in the orbit propagation model of low earth orbiting satellites [36]. The drag acceleration vector, \vec{a} , acting on a satellite can be related to several satellite and orbital properties and to the atmospheric mass density, ρ , by the following equation:

$$\vec{a} = -1/2(C_D A_{ref}/m)\rho|\vec{V}|\vec{V} \quad (1)$$

where C_D is the coefficient of drag, A_{ref} is the reference satellite area projected into the ram direction, m is the satellite mass, and \vec{V} is the satellite velocity vector with respect to the atmosphere. Changes in neutral density typically contribute the most to the total variability of drag acceleration, however, the $(C_D A_{ref}/m)$ term and thermospheric winds (entering through the $|\vec{V}|\vec{V}$ term) can also contribute significant amounts at times.

The thermosphere is a strongly driven dynamic system. Variations of neutral density in the thermosphere depend not only on location but on solar and geophysical conditions as well. Satellite accelerations can exhibit changes of more than an order of magnitude over the course of an 11-year solar cycle, and of a factor of 2-4 during moderate geomagnetic events with an approximate time-scale of 1-2 days. During geomagnetic storms, the spatial distribution and temporal response strongly depends on latitude and local time, both in geographic and magnetic coordinates.

The Air Force Space Command (AFSPC) requires accurate knowledge and forecasting of neutral density between 90 and 500 km. This requirement is focused on improving the efficiency of satellite catalog maintenance, the accuracy of reentry predictions, and the reliability of satellite conjunction analysis. In support of this goal, the current pursuit focuses on the incremental improvement of calibration techniques for semi-empirical thermospheric models. This is accomplished by finding the Principal modes of the thermosphere as defined by a physics-based model. This model-driven approach is taken to avoid the obstacles of insufficient data coverage that are encountered when constructing orthogonal functions using data-driven techniques [see 38, 32, 39].

2.2 Methods, Assumptions, and Procedures

2.2.1 The Jacchia Semi-Empirical Model

The Jacchia 1970 model (J70 hereafter) [22] is a static diffusion model of the upper atmosphere. The thermospheric portion of the model begins at 105 km. Above this level, J70 specifies the total number density, n_i , of each species, $i = \{\text{Ar, He, N}_2, \text{O, or O}_2\}$, by vertically integrating the diffusion equation:

$$\frac{dn_i}{n_i} = -\frac{m_i g}{k_B T} dz - \frac{dT}{T} (1 + \alpha_i) \quad (2)$$

where m is the molecular weight, g is the acceleration due to gravity, z is the height, k_B is the Boltzmann constant, T is the temperature, and α is the thermal diffusion coefficient (α assumed

to be -0.38 for He and 0 for all other species). The total mass density, ρ , can be calculated as the summation of the individual mass densities of each species: $\rho = \sum_i n_i m_i / N_A$, where N_A is Avogadro's number. The vertical temperature profile, $T(z)$, required to carry out the integration in (2) is parameterized in the following form:

$$T(z) = T_x + A \arctan \left\{ \frac{G_x}{A} (z - z_x) [1 + B(z - z_x)^j] \right\} \quad (3)$$

where $A = \frac{2}{\pi}(T_\infty - T_x)$, $B = 4.5 \times 10^{-6} \text{ km}^{-1}$, T_x is the temperature at a prescribed inflection point $z_x = 125 \text{ km}$, G_x is the temperature gradient at the inflection point, T_∞ is the exospheric temperature, and j is set to 2.5. With the application of several additional constraints [see 22], the model produces a vertical density profile that is uniquely specified by T_x and T_∞ . These temperatures have been fit to satellite drag data and are represented by parametric functions of solar flux, geomagnetic activity, latitude, and apparent solar local time.

Marcos et al. [37] first attempted to calibrate this model by estimating a global correction to the nighttime minimum value of T_∞ , designated as ΔT_c , to bring the model into better agreement with recent satellite tracking data. *Storz et al.* [69] extended this technique by estimating a spherical harmonic (SH) field for ΔT_c as well as for a correction to the value of T_x , designated as ΔT_x . Both global temperature corrections take the following form:

$$\Delta T(\varphi, \theta) = \sum_{l=0}^{\infty} \sum_{m=0}^l \bar{P}_l^m(\sin \varphi) \{C_l^m \cos m\theta + S_l^m \sin m\theta\} \quad (4)$$

where the \bar{P} 's are orthonormalized associated legendre polynomials of degree and order $[l \times m]$, the C 's and S 's are the expansion coefficients with S_l^0 omitted, φ is latitude, and θ is local time. It should be noted that with the application of the ΔT_c SH correction, the variable T_c is no longer a constant over the globe and hence can no longer be defined as the nighttime minimum value of T_∞ . The choice of correcting T_c , as opposed to T_∞ which is already a global field, is the convention chosen by AFSPC, and one to which we adhere in order to directly compare our model with the existing model. To facilitate comparison of the individual functions of an SH expansion with those of other functional expansions whose indices increase linearly, we define the 'mode number' to be used throughout this chapter. In the case of the SH functions, each mode corresponds to a single term within Equation 4 in the order of the summations, with the cosine terms preceding the sine terms for each degree and order. For instance, the expansion coefficients of modes 1-4 of the SH expansion functions would be C_0^0 , C_1^0 , C_1^1 , and S_1^1 , respectively.

Due to the sparse data sets available for near real-time estimation of the SH expansion coefficients, it was necessary to truncate the SH functions in Equation 4 for degree and orders higher than $[2 \times 2]$ (mode 9) for ΔT_c and $[1 \times 1]$ (mode 4) for ΔT_x . This extension has come to be known as the High Accuracy Satellite Drag Model (HASDM). The goal of our study is to replace the truncated set of SH functions used to specify ΔT_c and ΔT_x with a global basis set that more accurately represents the true variability of the thermosphere.

2.2.2 The TIE-GCM First-Principles Model

The Thermosphere-Ionosphere-Electrodynamics General Circulation Model (TIE-GCM) [59], developed by the National Center for Atmospheric Research (NCAR), is a comprehensive, first-

principles, three-dimensional, non-linear representation of the coupled thermosphere and ionosphere system that includes a self-consistent solution of the middle and low-latitude dynamo field. The model solves the three-dimensional momentum, energy and continuity equations for neutral and ion species at each time step, using a semi-implicit, fourth-order, centered finite difference scheme on each pressure surface in a staggered vertical grid. It can be run in either serial or parallel mode on a variety of platforms, including Linux workstations and supercomputers [<http://www.hao.ucar.edu/modeling/tgcm/tie.php>, accessed 24 Aug 2015].

The default model time step of 120 seconds is used when solving the time-dependent equations; however, in order to maintain a manageable amount of data the output is only recorded every hour for the purposes of this study. The horizontal grid spacing is 5° in latitude and longitude, with a vertical spacing of a half scale height. In this configuration, the model has 29 pressure surfaces covering the altitude range from 97 km to 500-700 km depending on solar activity. The external forcing of the TIE-GCM are solar irradiance [66], auroral electron precipitation [61], ionospheric convection driven by the magnetosphere-ionosphere current system [76], the amplitudes and phases of tides from the lower atmosphere [11], and the lower boundary parameterization of eddy diffusivity [50].

2.2.3 Construction of Basis Functions

The end product of this study is a subroutine that operates in much the same way as the J70 Dynamic Calibration Atmosphere (J70DCA) model [69]. However, we establish an improved set of basis functions to more efficiently and accurately correct the J70 model in the presence of recent satellite data. The desired basis functions should have the ability to represent the behavior of the thermosphere over a wide range of geophysical conditions. To that end, we have chosen to simulate such conditions using the TIE-GCM, then to fit the output to the low-dimensional J70 model, and finally to analyze the principal components of the fit parameters. The remainder of this section gives an in-depth explanation of this technique and a description of the resulting basis functions.

We initially ran the TIE-GCM during the entire year of 2004. However, because we desire a more general set of basis functions, and not one capable only of replicating the exact thermospheric conditions present in a free run of the TIE-GCM during a single year, we ran an ensemble of the TIE-GCM. For each of the 30 ensemble members, a distinct multiplicative factor is applied to the $F_{10.7}$ solar flux, the Joule heating, and the eddy diffusivity. These parameters are chosen to account for any natural variability of the input forcing and lower boundary conditions, as well as to mitigate any internal errors within the model. Within each ensemble member, a random multiplicative constant is applied over all of 2004 for each of the three adjustable parameters. Because the multiplicative factors are static in nature, they are not able to simulate, for instance, the transient response of the thermosphere during geomagnetically disturbed times. Instead, this behavior is reproduced by the input timeseries of Interplanetary Magnetic Field (IMF) observations coupled with the high-latitude ionospheric convection model of *Weimer* [76]. The role of the adjustable Joule heating parameter, however, is to enable the ensemble to simulate storms both smaller and larger than those that actually occurred during 2004.

While the nature of solar flux variability can be quantified given the relatively long record of historical data, variability of the other two chosen parameters is somewhat unobserved. Because of this, the choice of a probability density function (PDF) from which to draw these random en-

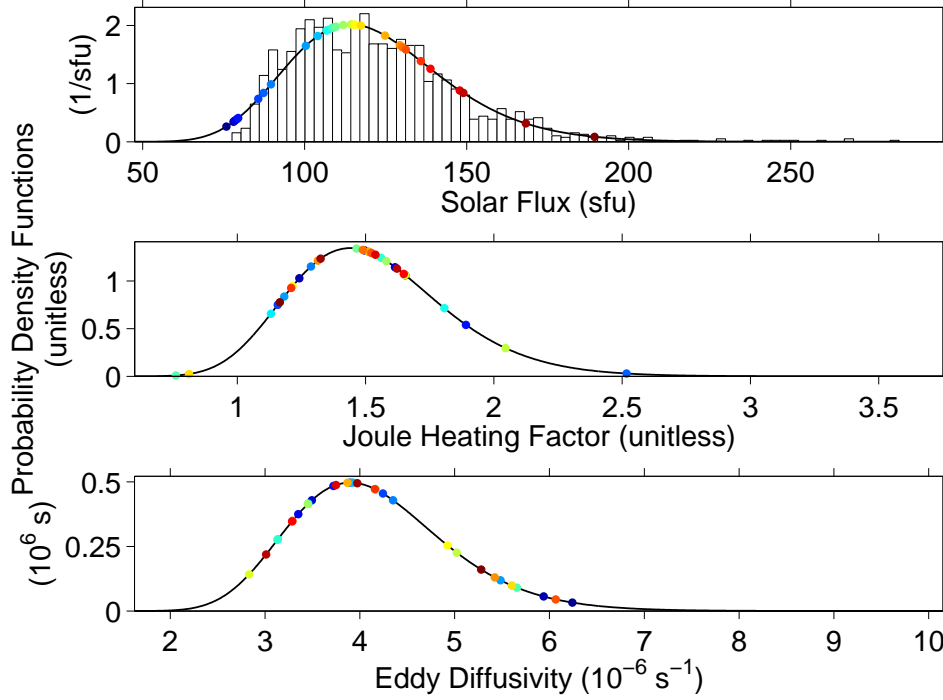


Figure 1: Distribution of ensemble parameters. Ensemble input parameters $F_{10.7}$ (top), Joule heating (middle), and eddy diffusivity (bottom) after application of randomly generated multiplicative factors. The histogram (top only) shows historical data from 2004-like years within the last 5 solar cycles, black lines show the corresponding PDFs, and color-coded dots indicate the random values generated for each ensemble member. The histogram and all PDFs have been normalized such that the integrated area under the curve is equal to 1.

semble parameters is somewhat arbitrary. Nevertheless, certain properties were desired when choosing the PDF of the multiplicative factors. Among these were: (1) coverage over the interval $(0, \infty)$, (2) the ability to represent skewness in data, and (3) probability $\Pr[X \geq a] = \Pr[X \leq 1/a]$ for all $a \geq 1$. The second property gives the ability to more closely represent the positive skewness seen in historical solar flux data during a given phase of the solar cycle. The third property ensures, for example, that the probability of generating a multiplicative value of $1/2$ or smaller is the same as that of generating a value of 2 or larger. Given these desirable properties, a natural choice for the PDF is a zero-mean log-normal distribution: $\ln \mathcal{N}(\mu=0, \sigma^2)$. In the case of solar flux, the log-normal parameter σ can be fit to the timeseries of $F_{10.7}$ from the past 5 solar cycles during years which correspond to the same phase of the solar cycle as 2004. Using the maximum likelihood technique, a standard deviation of $\sigma=0.20$ was estimated. The top panel of Figure 1 shows the histogram of historical data for 2004-like years along with the resulting PDF of simulated $F_{10.7}$ calculated for a day in which the measured solar flux is equal to the median of the selected historical data (i.e. $F_{10.7}=118.8$ sfu). The log-normal PDF fits the historical data reasonably well, accounting for the extended upper-tail as well as the sudden drop-off near 80 sfu. The color-coded dots show the values of $F_{10.7}$ that would be generated for the ensemble during this day.

Similar arguments were used in the construction of the remaining two PDFs. However, without the aid of data, there was little hope of establishing an accurate PDF for the Joule heating or eddy diffusivity multiplicative factors. Therefore, the same σ parameter was used for all three PDFs. In theory, the σ parameters for the latter two PDFs could be adjusted to yield the best agreement with neutral density or satellite drag data; however, this process was deemed computationally impractical. Moreover, the exact shape of the PDF should not have a critical effect on the overall structure of the resulting basis functions. The middle panel of Figure 1 shows the PDF and randomly generated ensemble values for the Joule heating multiplicative factor, taking into account the TIE-GCM's default value of 1.5. Finally, the lower panel shows the same data for eddy diffusivity during a day in which the default value equals the baseline of the model of *Qian et al.* [50] (i.e. $K_E=4.06\times10^{-6}s^{-1}$).

After simulating a wide range of conditions, we then fit the TIE-GCM output neutral mass density to the J70 model making use of the adjustable parameters ΔT_c and ΔT_x . To accomplish this, J70 is used in a similar fashion to the method of *Storz et al.* [69]; however, instead of estimating SH expansion coefficients, ΔT_c and ΔT_x are estimated directly at each latitude/local time grid point of the TIE-GCM using the vertical profile of mass density from 200 km to the upper boundary of the TIE-GCM. Here the native longitude grid of the TIE-GCM is transformed into a local time grid using the simple equation $\theta = UT + lon/15 \pmod{24}$, ignoring the +16/-14 minute offset of local noon over the course of the year [65]. (Note: this omission can easily be remedied in future model versions by performing this fitting procedure in the appropriate functional domain as opposed to the gridded domain). Figure 2 shows this basic process for one time step within one ensemble member and at one location in latitude and local time. An iterative nonlinear least-squares fit is employed to bring the original J70 log-density profile into agreement with the TIE-GCM log-density vertical profile. This procedure requires knowledge of the partial derivatives $\partial\rho/\partial T_c$ and $\partial\rho/\partial T_x$ with respect to the J70 model at each location and height, which are calculated by the J70DCA algorithm [69]. For each TIE-GCM model time step and ensemble member, this produces a map of ΔT_c and ΔT_x on the latitude/local time grid of the TIE-GCM (such as those shown in the left panels of figures 6 and 7).

It should be noted that the fits of the TIE-GCM vertical profile to J70 are not perfect. In particular, there is no guarantee that improving the agreement of the vertical mass density profiles between J70 and TIE-GCM will also improve the agreement of the vertical temperature profiles. This behavior is caused by several of the assumptions of J70 that are inconsistent with the TIE-GCM. Among these is J70's governing assumption of diffusive equilibrium above 105 km, which is not strictly obeyed by the TIE-GCM. Photochemical production/loss, turbulent diffusion in the lower thermosphere, upwelling [60] and horizontal transport [10] all commonly cause departures from diffusive equilibrium within the TIE-GCM. Additional J70 assumptions of consequence include a constant lower boundary condition for mass density, temperature and mixing ratios at 90 km, an imposed static model describing the dissociation of molecular oxygen below 105 km, an instantaneous transition from turbulent mixing to diffusive equilibrium at 105 km, and a temperature profile that obeys Equation 3. Therefore, in the context of this study, the adjusted temperature profile of J70 should be regarded as a mathematical construct whose physical interpretation is limited by the degree to which the TIE-GCM mimics the aforementioned assumptions at any given time.

Through analysis of the ΔT_c and ΔT_x corrections, we can capture the most significant modes of variability using the principal component analysis technique [see 49]. Principal component

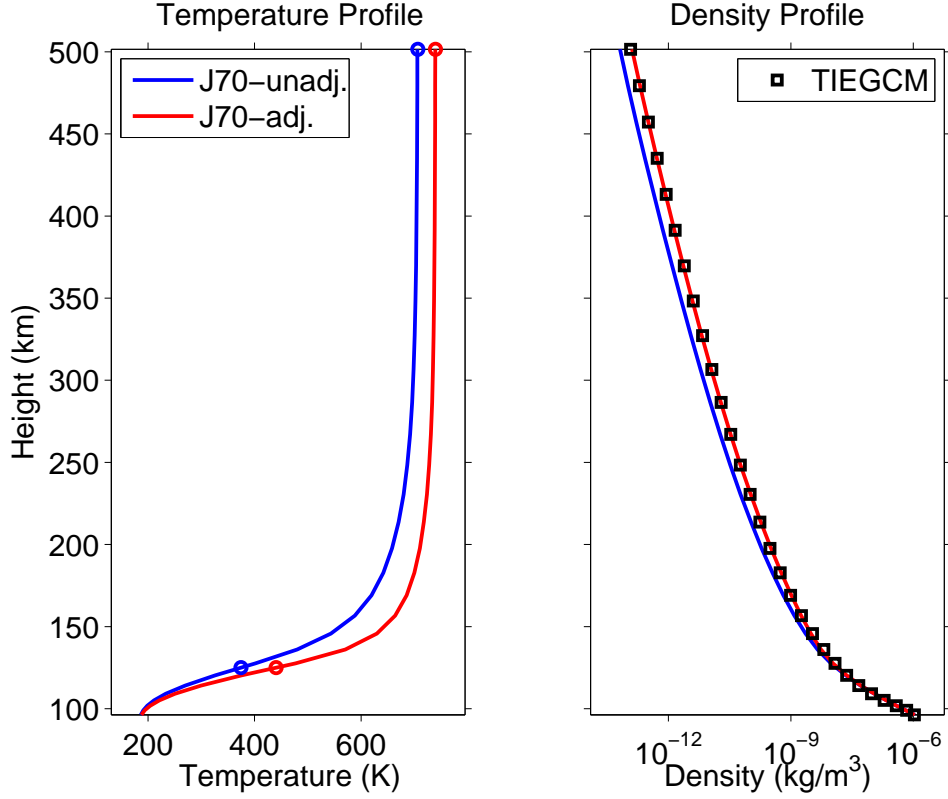


Figure 2: Temperature/density vertical profile . Temperature (left) and density (right) vertical profiles for the TIE-GCM (black squares, density only), J70-unadjusted (blue), and J70-adjusted (red) at one latitude/local time grid point. Circles indicate unadjusted and adjusted T_x at 125 km and T_∞ near the upper boundary.

analysis is a linear technique that provides the optimal set of basis functions with which to represent the covariance matrix of a data set or model output. Rearranging the ΔT_c and ΔT_x fields into an m -by- n matrix called F , m being the number of time steps ($m=366 \text{ days} \times 24 \text{ hours} \times 30 \text{ ensembles}=263,520$) and n being the number of unique grid point locations ($n=36 \text{ latitudes} \times 72 \text{ local times}=2,592$), we compute the n -by- n quasi-covariance matrix $R = F^T F$. At this point, we solve the matrix eigenvector/eigenvalue problem: $R\Psi = \Psi\Lambda$, where Ψ is a matrix containing the column eigenvectors, Ψ_i , of R , and Λ is a diagonal matrix formed from the eigenvalues, λ_i , of R . The eigenvectors, Ψ_i , are referred to as Principal Component (PC) expansion functions, while the eigenvalues relate to the amount of variance of the original fields that is captured by each corresponding eigenvector. This amounts to finding the set of orthonormal basis functions that maximizes the projection of the row-vectors of F onto each basis function. In addition to providing an optimal representation of the covariance matrix, R , a coefficient expansion with all n eigenvectors is also capable of representing any data on the latitude/local time grid, including all data contained in the F matrix. This is simply a direct consequence of the orthonormality of the eigenvectors and could be said of any basis set defined on the same grid. However, the usefulness of the eigenvectors comes from the fact that most of the variability in F can be recovered using only a handful of the eigenvectors, which cannot be said of many other basis sets.

2.3 Results and Discussion

The PC procedure is carried out separately for the ΔT_c and ΔT_x fields. Figures 3 and 4 show the first 9 PC expansion functions for ΔT_c and the first 4 PC expansion functions for ΔT_x , respectively, after rearranging into the latitude/local time coordinate frame. The different modes are a combination of the true thermospheric variability with the error in both the TIE-GCM and J70. Much of the variability caused by physical processes that cannot be captured by the original J70 model – even when corrected by a truncated SH expansion – can be represented by the PC expansion functions. More importantly, the cumulative fraction of the variance, R , captured by each mode approaches 1 much more quickly for the PC expansion than it does for the SHs, as shown by figure 5. In fact, if we were to attempt to capture the same amount of variance as the first PC expansion function of ΔT_c and ΔT_x using a truncated SH expansion, we would require the expansion functions through degree and order $[6 \times 0]$ (37 modes) and $[2 \times 0]$ (5 modes), respectively.

The first mode of PC expansion functions accounts for 98.1 and 87.8% of the total variance in the TIE-GCM ΔT_c and ΔT_x maps, respectively, as shown in Figure 5. Both expansion functions have a strong mean bias, indicative of the ability to correct the J70 model bias. In general, the PC expansion functions are a convolution of model error – introduced by the TIE-GCM as well as by J70 – with the true thermospheric variability, and are not necessarily physically significant in spite of their mathematical significance. However, some information on thermospheric variability can still be gleaned from several of the lowest modes. For instance, modes 1, 3 and 4 of ΔT_c (Figure 3) have a strong diurnal component at low to mid-latitudes. Mode 2 has a strong semidiurnal component evident at low to middle latitudes, giving way to a latitudinally antisymmetric seasonal component near the poles. Modes such as 6 and 7 give the appearance of having a strong diurnal variation that maximizes near 60° latitude in the southern hemisphere. In this region, the phase offset between the two modes is approximately 6 hours in local time, which allows for any phase and amplitude to be represented by the appropriate linear combination. Given their non-stationary nature with respect to local time, these functions are more likely to be associated with the longitude-UT effect [see 17] related to the offset between the geographic and geomagnetic poles, an effect that isn't well represented by the longitudinally-independent J70 model formulation or by HASDM. For ΔT_x (Figure 4), mode 1 has a strong diurnal component, however the latitudinal structure is unique from modes 1, 3 or 4 of the ΔT_c PC expansion functions. Mode 2 for ΔT_x is strikingly similar to mode 2 for ΔT_c , but with an increased latitudinal range of the semidiurnal feature and an antisymmetric feature that is subdued in the southern hemisphere.

For an initial comparison of the performance between the new and currently-used basis functions, we reconstruct the ΔT_c and ΔT_x fields from one of the TIE-GCM ensemble members using both methods. In order to show improvement in neutral mass density specification, we also reconstruct the density at an altitude of 400 km using both methods. The $[2 \times 2]$ SH representation of ΔT_c uses 9 orthogonal functions while the $[1 \times 1]$ SH representation of ΔT_x uses 4 orthogonal functions. To stay consistent with the approach used by HASDM, we also limit the PC expansion to 9 functions representing ΔT_c and 4 functions representing ΔT_x . At each time step of the TIE-GCM ensemble member, the truncated set of expansion functions can be fit to the ΔT_c and ΔT_x fields using a least squares method to estimate the expansion coefficients, C_i , in the following

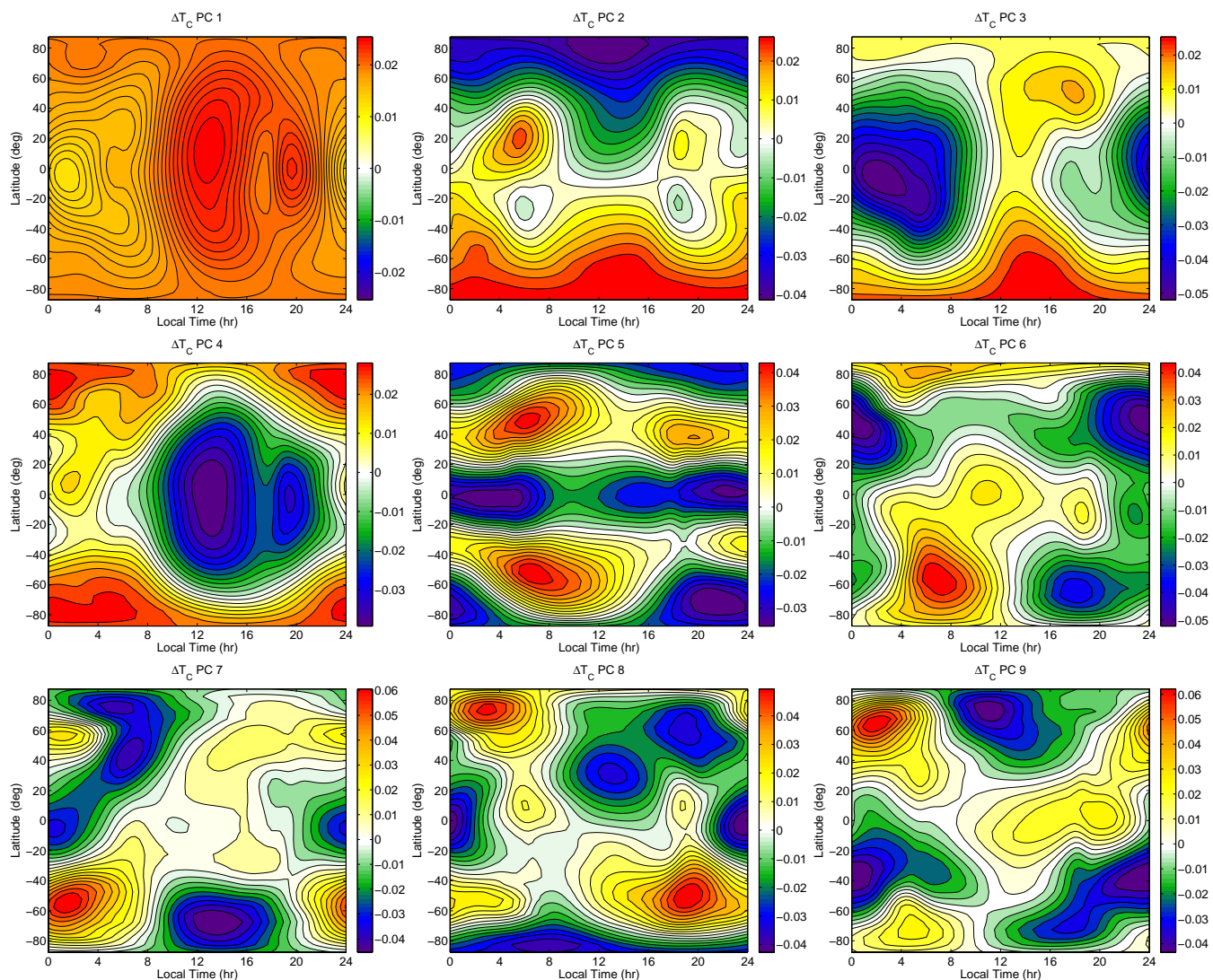


Figure 3: ΔT_c expansion functions. First 9 modes of the PC expansion functions of ΔT_c estimated for the TIE-GCM during 2004. Each PC expansion function is normalized such that $\Psi_i^T \Psi_i = 1$.

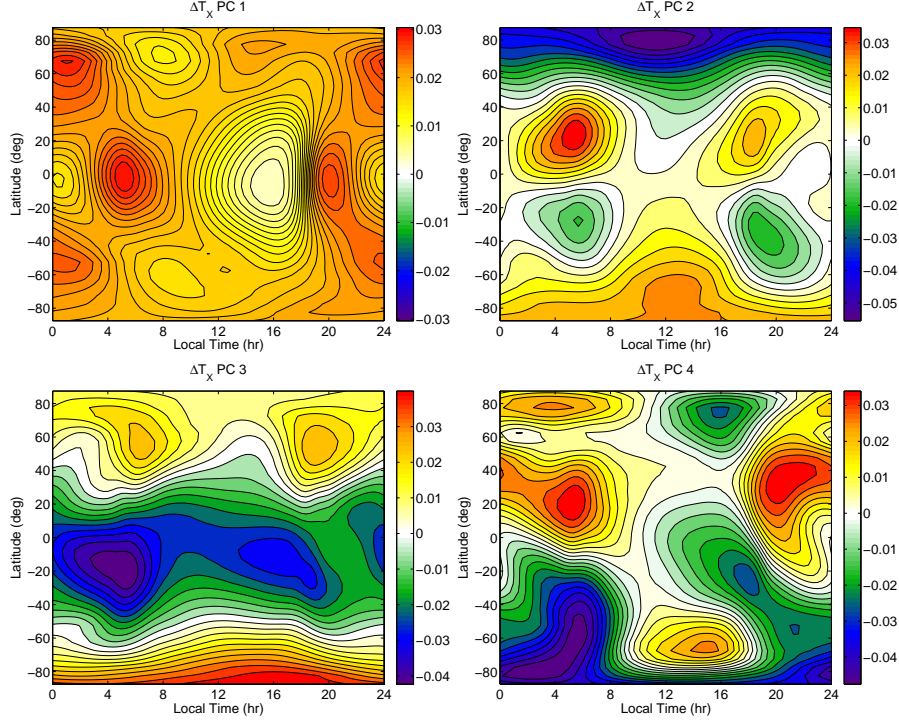


Figure 4: ΔT_x expansion functions. First 4 modes of the PC expansion functions of ΔT_x estimated for the TIE-GCM during 2004. Each PC expansion function is normalized such that $\Psi_i^T \Psi_i = 1$.

formula:

$$\Theta(\varphi, \theta) = \sum_i C_i \Theta_i(\varphi, \theta) \quad (5)$$

where Θ is the reconstructed field (representing either ΔT_c or ΔT_x), the Θ_i 's are the expansion functions (either PCs or SHs), φ is latitude, θ is local time, and the subscript i refers to the mode of the expansion function. Density at 400 km is then calculated from J70 modified by the reconstructed ΔT_c and ΔT_x fields. Figure 6 shows the original ΔT_c field estimated using the TIE-GCM neutral density as input data, as well as the fits using modes 1-9 of the PC and SH expansions. Figure 7 shows a similar fit for ΔT_x using modes 1-4. Figure 8 shows the total mass density, ρ , at 400 km as simulated by the TIE-GCM and reconstructed using the PC and SH expansion functions. The epoch for figures 6, 7, and 8 was chosen such that the performance of the truncated SH expansion is typical of all 2004.

To compare the PC reconstructions to the baseline SH reconstructions of ΔT_c , ΔT_x and ρ at 400 km, we employ a relative Root Mean Squared error (rRMSe) metric, expressed as a percentage increase or decrease in the RMS error:

$$\text{rRMSe} = -100 \times \left(\sqrt{\frac{\sum_{\varphi} \sum_{\theta} (\Theta_{\text{PC}}(\varphi, \theta) - \Theta_{\text{TIE-GCM}}(\varphi, \theta))^2}{\sum_{\varphi} \sum_{\theta} (\Theta_{\text{SH}}(\varphi, \theta) - \Theta_{\text{TIE-GCM}}(\varphi, \theta))^2}} - 1 \right) \quad (6)$$

where Θ_{PC} and Θ_{SH} represent the reconstructed fields (either ΔT_c , ΔT_x or ρ at 400 km) using the

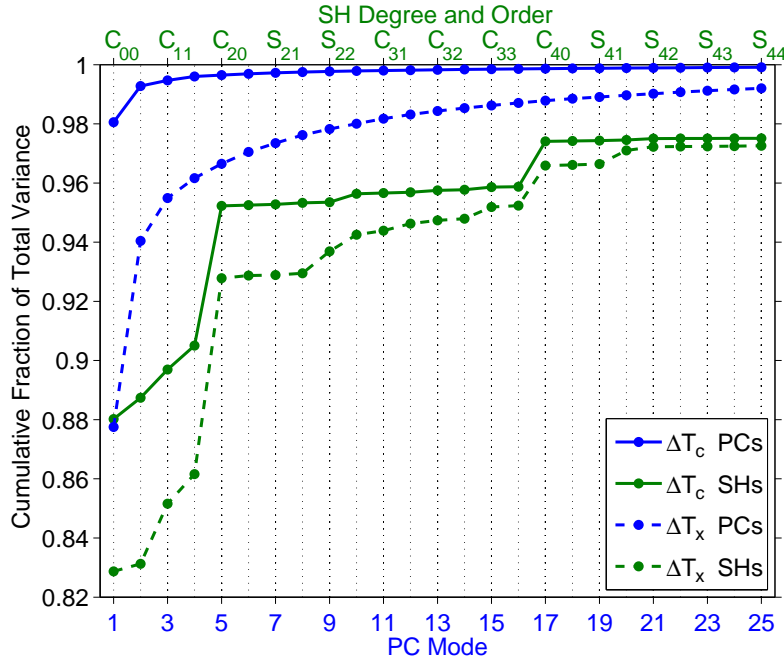


Figure 5: Cumulative fractional variance. Cumulative fractional variance of the ΔT_c (solid) and ΔT_x (dashed) TIE-GCM fields that is recovered by the PC (blue) and SH (green) expansion functions by mode number. Note that the first 25 SH modes are equivalent to an expansion through degree and order $[4 \times 4]$.

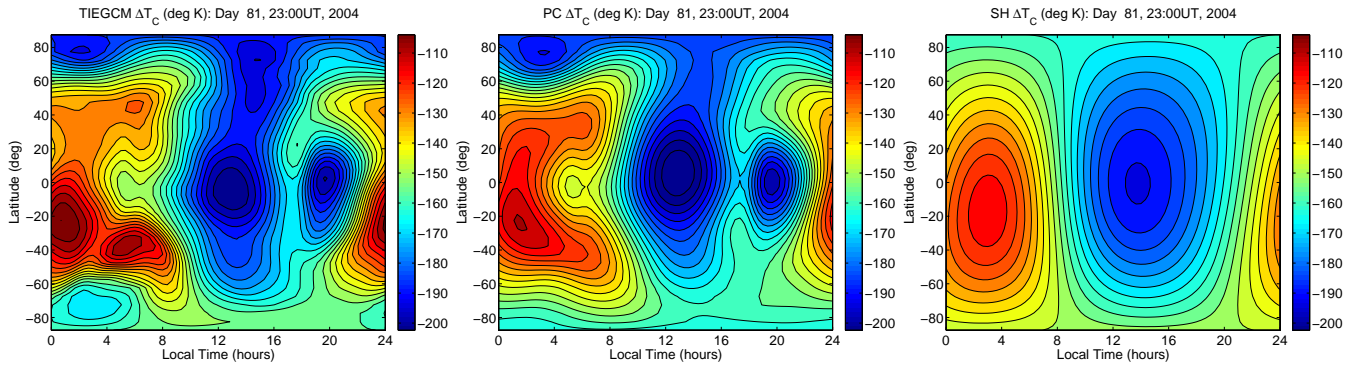


Figure 6: ΔT_c reconstruction. ΔT_c estimated for the TIE-GCM for a typical time epoch in 2004 (left), the reconstruction of ΔT_c using the 9 lowest order PC expansion functions (center), and the reconstruction of ΔT_c using a $[2 \times 2]$ (9 modes) SH expansion functions (right).

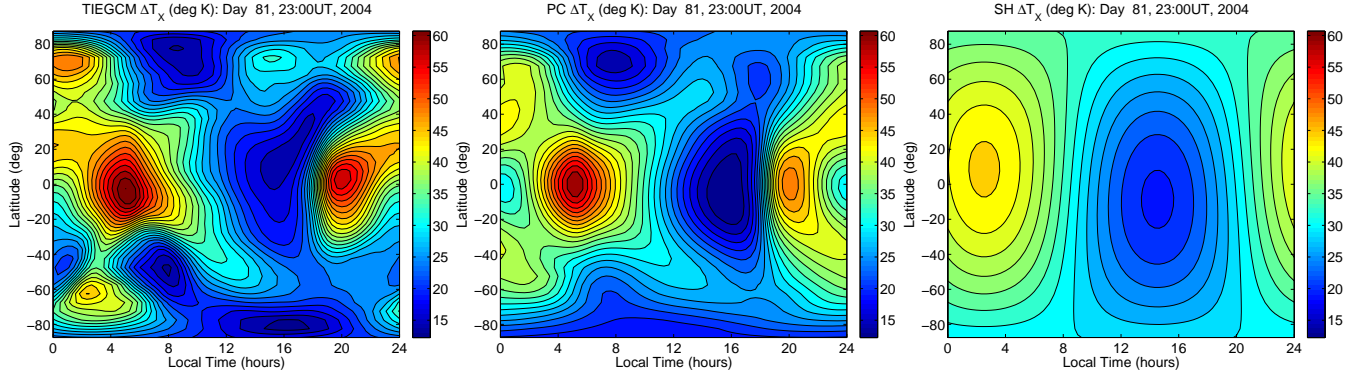


Figure 7: ΔT_x reconstruction. ΔT_x estimated for the TIE-GCM for a typical time epoch in 2004 (left), the reconstruction of ΔT_x using the 4 lowest order PC expansion functions (center), and the reconstruction of ΔT_x using a $[1 \times 1]$ (4 modes) SH expansion functions (right).

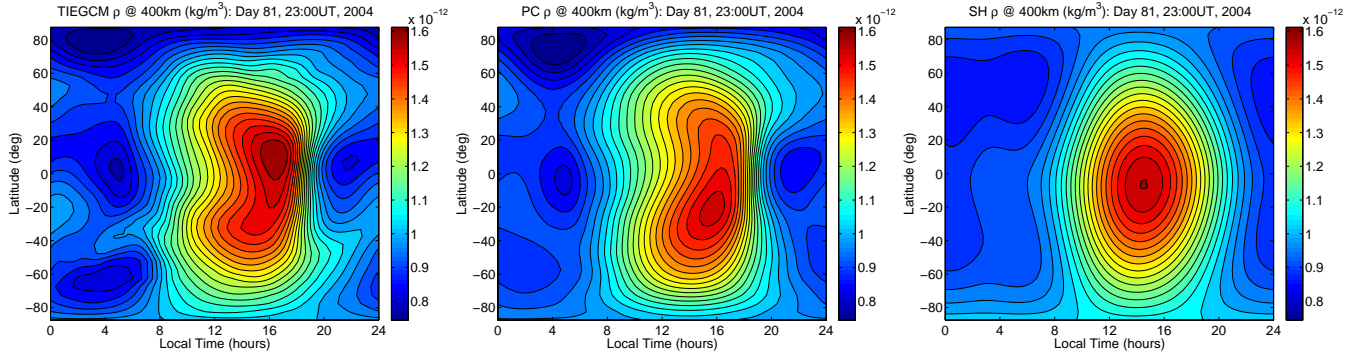


Figure 8: Neutral Density reconstruction. Neutral density, ρ , at 400 km estimated for the TIE-GCM for a typical time epoch in 2004 (left), and the reconstructions of ρ at 400 km using PC expansion functions (center) and SH expansion functions (right).

subscripted method, and $\Theta_{\text{TIE-GCM}}$ represents the corresponding field as calculated directly from the TIE-GCM. The negative sign is used so that positive rRMSe values indicate an improvement over the performance of the SH expansions. For the reconstructions of ΔT_c in figure 6, the RMS error improved by 52.5% when using the PC approach instead of the SH approach. For the reconstructions of ΔT_x in figure 7, the RMS error improved by 38.7%. As for the reconstructions of ρ at 400 km altitude shown in figure 8, the RMS error improved by 49.0% during this time period.

Figure 9 shows the 27-day smoothed rRMSe throughout 2004 for the ΔT_c and ΔT_x fields. On average, the PC reconstructions of ΔT_c and ΔT_x reduce the RMS by 44.8% and 45.1%, respectively, over the SH reconstructions. Also shown in Figure 9 is the 27-day smoothed rRMSe for ρ at 400 km. The PC reconstructions of ρ reduce the RMS by 32.9% on average for all of 2004.

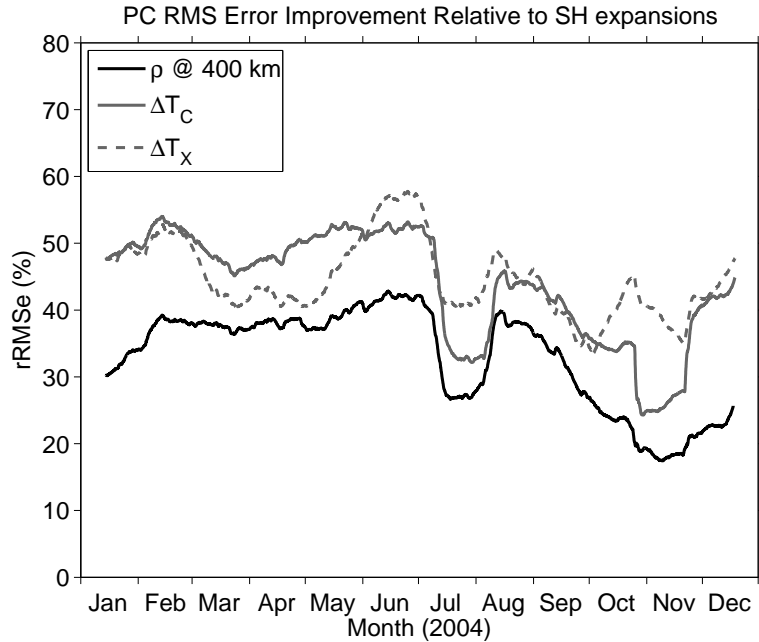


Figure 9: Relative RMS error. 27-day smoothed RMS error of the PC reconstructions of ρ at 400 km (black line), ΔT_c (grey line), and ΔT_x (grey dashed line) relative to RMS error of the SH reconstructions. Positive values indicate that the PC reconstructions are outperforming the SH reconstructions.

2.4 Conclusions

We have presented a new set of basis functions capable of representing the most important modes of thermospheric variability within the framework of an adjusted static diffusion model. Our approach demonstrates the potential for significant upgrades to current operational satellite drag modeling capabilities, while circumventing many of the technical and practical issues currently limiting data assimilation with physics-based models. Thermospheric variability is specified by the TIE-GCM, and thus, several limiting assumptions should be pointed out. First, the simplifying assumptions of hydrostatic equilibrium and constant gravity are imposed. Secondly, several physical processes are not fully accounted for, such as the influences of the lighter neutral and ion species, [H] and [He]. In addition, eddy diffusivity at the lower boundary is specified by an empirical parameterization. In spite of these and other simplifying assumptions along with the subsequent error that they impose on the TIE-GCM, the modes of variability of the TIE-GCM are more realistic than any existing empirical model. The purpose of this study is to extract the most important of these modes and use them to efficiently calibrate empirical models, without the increased data coverage and overhead that would be required to calibrate a high-dimension general circulation model such as the TIE-GCM.

The validation presented in this chapter is only a first step. A comparison of the new and currently-used techniques using actual satellite tracking data will be required before this basis set can be considered validated. As mentioned in Section 3, several of the PC modes exhibit traits which are not included in the J70 model, e.g. the longitude-UT effect. Thus we are able

to include and correct for modes of thermospheric variability not captured the current implementation of HASDM. However, some of these traits may not be observable from the ground-based satellite tracking data set currently used to drive HASDM. Validation studies with these ground-based satellite tracking data is needed to resolve such issues, as well as guide any necessary modifications to the PCs to provide the needed upgrade to operational satellite drag modeling capabilities.

3 First-Principles Helium Model

3.1 Background

The presence of helium as a major component in the Earth's upper thermosphere and lower exosphere was first inferred from measurements of satellite drag. By analyzing orbital variations of the Echo 1 satellite orbiting above 1000 km, *Nicolet* [47] reasoned that atomic oxygen was incapable of producing the observed satellite deceleration given reasonable values of exospheric temperature. Likewise, atomic hydrogen concentrations were thought to be much too low to create such a deceleration.

Increasingly direct evidence of helium's presence soon emerged from *in situ* mass spectrometer measurements taken onboard Explorer 17 [54]. Concomitant with this confirmation was the hint of a significant seasonal-latitudinal variation in the helium distribution, relative to the other measured constituents (i.e. molecular nitrogen and atomic oxygen). Soon thereafter, strong semi-annual variations inferred from the satellite drag acting on Echo 2 [6] around 1100 km were linked to seasonal variations of helium concentration. *Keating and Prior* [26] confirmed this result with satellite drag data from the Explorer 9, 19, and 24 satellites. They also noted an apparent enhancement near the winter pole, which they termed the "winter helium bulge," with an approximate winter-to-summer ratio of 2.5. Subsequent drag-inferred calculations by *Keating et al.* [27] yielded ratios in excess of 3 at an altitude of 850 km.

Reber et al. [55], using mass spectrometer measurements from the Ogo 6 satellite, showed an order-of-magnitude difference between the helium content in winter and summer hemispheres near 400-600 km altitude. This disagreement with previous results highlighted the limitations of the drag-inferred technique, specifically, reliance on the assumption of diffusive equilibrium to separate composition-induced mass density variations from those caused by temperature. In response, *Keating et al.* [28] augmented their drag-inferred technique to include a description of the background composition that was consistent with the available mass spectrometer data. New ratios in excess of an order of magnitude could then be obtained through this method as well. In addition to establishing a larger bulge ratio, *Reber et al.* [55] noted a strong correlation of the maximum helium density with the location of the winter geomagnetic pole. This was interpreted as a sensitivity of the helium distribution to the thermospheric wind system.

In addition to high-latitude variations near the solstices, *Newton et al.* [46] detected a strong local time preference for helium concentration as measured by mass spectrometers on the low-inclination San Marco 3 satellite. *Reber et al.* [56] and *Mayr et al.* [44] discussed similar variations manifest within the Ogo 6 density model [16]. These findings showed a preference of the diurnal maxima toward earlier times for species with small molecular masses, with the opposite being true for species of large mass. The San Marco 3 observations, taken at altitudes near 225 km, showed a preference toward the 06-09 LT sector while those taken by Ogo 6, near 450 km, showed maxima closer to 10 LT.

The realization of these phenomena motivated several modeling studies to uncover the mechanism responsible for the counterintuitive distribution of helium in the thermosphere. Noticing that helium vertical profiles measured by several rocket-based mass spectrometers departed quite drastically from diffusive equilibrium, an early study by *Kasprzak* [25] invoked an additional diffusive flux in order to reconcile the observations with his model. This treatment required

vertical fluxes on the order of 6×10^8 and $2 \times 10^{10} \text{ cm}^{-2}\text{s}^{-1}$ for summer and winter conditions, respectively, over an altitude range of 120–200 km. *Kockarts* [31] later noted, however, that these values were larger than the maximum flux allowed by molecular diffusion, thus requiring an additional mechanism of transport.

Johnson and Gottlieb [23] used basic considerations of continuity to show that a general summer-to-winter flow of the major atmospheric constituents could account for a buildup of helium in the winter polar regions. Without discounting these findings, several attempts were made to ascertain the effect of atmospheric fluctuations on helium transport. *Hodges* [19] modeled large-scale fluctuations as monochromatic plane waves, which effected a downward transport and an overall decrease to the scale height of species with masses smaller than the mean mass. Similarly, *Kockarts* [30] derived the eddy diffusivity profile necessary to reconstruct the winter helium bulge observations of *Reber et al.* [55], under the assumption of molecular diffusion in the absence of wind. Results from these studies suggested that eddy diffusion could in fact control the global helium distribution. However, recreating the observed winter bulge ratios required more than an order-of-magnitude increase in eddy diffusivity from winter to summer hemispheres. These results were qualitatively consistent with each other, yet they implied that similar latitudinal signatures should be evident in other minor atmospheric constituents, a feature that was inconsistent with previous observations of atomic oxygen [31].

Reber and Hays [53] performed a more rigorous treatment of the effects of circulation on the distribution of helium. Included in their model were the effects of molecular and eddy diffusion as well as a parameterized circulation pattern of the background gas that satisfied continuity requirements and could be tuned to simulate a given level of summer-to-winter flow. Combining the equations of continuity and momentum for a minor species led to an accurate representation of previous winter helium bulge observations. The idea that the winter helium bulge could be completely explained by seasonal circulation patterns led, however, to an apparent paradox. At times of high solar flux, when an enhanced summer-to-winter flow had been expected to occur, smaller pole-to-pole helium ratios had been observed. *Reber and Hays* [53] explained the discrepancy by invoking the mechanism of exospheric flow, whereby during times of high solar flux, increased temperatures in the upper thermosphere drive a larger exospheric flow directed away from the winter bulge. The balance between the circulation-induced effects and exospheric transport was found to control the magnitude of the latitudinal gradient in helium concentration that could be supported by the atmosphere.

By analyzing the combined equations of continuity and momentum for a minor species, *Reber and Hays* [53] and *Hays et al.* [12] identified the vertical advection term as being responsible for establishing the seasonal distribution of helium. In the presence of diffusively separated atmospheric constituents, this term leads to increased helium densities in regions of downwelling and decreased densities in regions of upwelling. The opposite behavior is implied for species, such as argon, that are heavier than the local mean mass. *Reber* [52] further explained that in order to perturb composition from the distribution prescribed under conditions of diffusive equilibrium, the vertical winds must be significant in relation to a characteristic vertical diffusive velocity, $v_D = D/H$, where D is the mutual diffusion coefficient and H is the atmospheric scale height.

Contemporaneous works by *Mayr and Volland* [42, 43] asserted a similar yet distinct perspective on the matter. *Mayr et al.* [45] summarized these findings and coined the phrase “wind-induced diffusion,” describing horizontal transport in the presence of diffusively sepa-

rated constituents. Both groups agreed that the interaction between helium and the background circulation—consisting of upwelling in the summer hemisphere, summer-to-winter flow, and downwelling in the winter hemisphere—would lead to a winter helium bulge consistent with observations. However, *Reber and Hays* [53] suggested that the transport mechanism was related to the vertical advective motion in the presence of diffusive separation, while *Mayr et al.* [45] believed horizontal bulk motion in the presence of diffusive separation to be responsible.

As the basic mechanism causing the observed helium behavior—i.e. circulation within a diffusively separated atmosphere—continued to mature, several successful satellite mass spectrometer missions served to refine these theories and document the phenomenological implications. The open source mass spectrometers on Atmospheric Explorer satellites (AE-C, -D, and -E) were used by several investigators to further quantify seasonal variations [40, 41, 2]. *Reber et al.* [57] also analyzed these data to study waves in composition, showing coherent phase relationships between the various constituents. *Hedin and Carignan* [15] used data from the Dynamics Explorer 2 (DE-2) satellite to show that even during geomagnetically quiet times, signatures of helium depletion are present near the magnetic poles. These data sets now comprise the majority of our understanding of thermospheric composition, the empirical basis of which is embodied by the Mass Spectrometer and Incoherent Scatter (MSIS) series of models [13, 14, 48], successors of the Ogo 6 model. More recently, *Thayer et al.* [74] inferred strong signatures of helium from differences in total mass densities measured at two different altitudes by high-precision accelerometers on board the Challenging Mini-Satellite Payload (CHAMP) and Gravity Recovery and Climate Experiment (GRACE) satellites [70]. *Liu et al.* [34] extended this work, showing that the response of the mass density vertical profile during a geomagnetic disturbance is quite sensitive to the atomic oxygen/helium transition height.

The remainder of this chapter is organized as follows. Section 3.2 introduces a self-consistent method for calculating helium abundances and transport by modifying an existing general circulation model of the thermosphere. Unlike previous formulations, we do not impose the assumption that helium remains a minor species throughout the model domain, which can have deleterious effects at high altitudes. Section 3.3 highlights the salient features of the new model, including helium's role in determining mean mass, total mass density, pressure level height and winds.

3.2 Methods, Assumptions, and Procedures

3.2.1 The TIE-GCM Baseline Model

The model developments described in this chapter have been applied to the National Center for Atmospheric Research Thermosphere-Ionosphere-Electrodynamics General Circulation model (NCAR/TIE-GCM) v.1.95 [63, 59], and are slated for inclusion in the next TIE-GCM and TIME-GCM [62] model versions. The TIE-GCM is a first-principles upper atmospheric general circulation model that solves the Eulerian continuity, momentum, energy, and composition equations for the coupled thermosphere-ionosphere system. The vertical coordinate is specified by log-pressure levels in half-scale height increments, providing coverage in altitude of approximately 97 km to 600 km, the latter being dependent on solar activity.

Tidal forcing at the lower boundary is specified by the Global Scale Wave Model [11]. Annual and semi-annual variations in sub-grid turbulent fluctuations are taken into account by applying

seasonal variation of the eddy diffusivity coefficient at the lower boundary [50, 51]. Based on measurements from the Mauna Loa Observatory [29], the mixing ratio of CO₂ imposed at the lower boundary was set to 364 ppmv for 1996, increasing linearly by 1.5 ppmv per year thereafter.

In the simulations presented throughout this chapter, solar irradiance is specified in a manner consistent with *Solomon et al.* [67]. The M_{10.7} index is used in place of the F_{10.7} solar proxy in an effort to better capture solar UV and EUV irradiance during the deep solar minimum of 2008. The M_{10.7} index derives from the magnesium core-to-wing (MgII c/w) of *Viereck et al.* [75] via a linear fit to the F_{10.7} proxy calculated during 1978–2007 [67]. With this normalization, M_{10.7} can be used in place of F_{10.7} to drive the EUVAC proxy model [see 58, 77, 66].

Magnetospheric inputs to the polar regions are specified by an applied electric potential pattern and an auroral precipitation oval. The *Heelis et al.* [18] empirical specification of magnetospheric potential in the ionosphere, which is parameterized by the 3-hour geomagnetic K_P index, is the standard TIE-GCM input and is employed for the simulations presented throughout this chapter. Auroral precipitation is applied as described by *Roble and Ridley* [61] based on the estimated hemispheric power of precipitating electrons. The empirical estimate of this power as it depends on K_P has been increased from its original formulation by a factor of ~2, based on results from the Global Ultraviolet Imager (GUVI) on the TIMED satellite [78].

The TIE-GCM uses the method outlined by *Richmond et al.* [59] to calculate the low-latitude ionospheric electrodynamics driven by conductances and neutral dynamics. The calculated electric potential is merged with the externally imposed potential within each polar cap, using cross-over boundaries that vary dynamically with the size of the magnetospheric potential pattern. See *Solomon et al.* [68], section 2.3, for further detail concerning the high-latitude inputs, and *Solomon et al.* [67], section 4, for a discussion of model uncertainties.

3.2.2 Implementing Helium as a Major Species

The equations describing the transport and concentration of the various components in the upper atmosphere are coupled to one another through diffusive and chemical processes. When solving for the concentration of a minor species [63], several terms in the fully coupled composition equation are assumed to be small. With the neglect of these terms, the solution of the major species composition becomes dynamically decoupled from that of the minor species composition, leading to a more efficient segmented numerical solution. The main terms that must be neglected are those in the diffusion matrix describing the acceleration experienced by any major species caused by collisions with the minor species as well as those that account for the effect that the minor species has on the mean mass and scale height of the atmosphere. It is straightforward to show that the effect of these terms is small when the mass mixing ratio of the minor species in question is also small. Helium as a minor species in the TIE-GCM was recently implemented by *Liu et al.* [35]. While this approach demonstrated the model's ability to accumulate helium in the winter hemisphere, it required the *ad hoc* inclusion of helium into the scale height calculation in order to avoid unrealistically high values during long simulations.

As a simple test, an empirical approach can be used to ascertain whether or not helium satisfies the assumptions necessary to treat it as a minor constituent. We employ the MSIS model [48], which represents helium abundance in an averaged sense as observed by mass spectrometer observations spanning several decades. However, care must be taken when converting between the vertical coordinate systems of MSIS and TIE-GCM. The TIE-GCM uses

log-pressure, $z = \ln(p_0/p)$, as its vertical coordinate, where p_0 is a reference pressure set to $5 \times 10^{-4} \text{ g}/(\text{cm} \cdot \text{s}^2)$. In order to obtain a reasonable estimate of the amount of helium that should be present within the vertical domain of the TIE-GCM, it is necessary to compute MSIS densities with respect to the TIE-GCM's log-pressure scale. Using the ideal gas law, we directly calculate the log-pressure level from the number densities and temperatures specified by MSIS.

As molecular diffusion becomes dominant with increasing height, a neutral species of comparatively small mass such as helium will increase in relative concentration. Due to the interaction between global circulation and molecular diffusive flow, the largest values tend to occur at high latitudes in the winter hemisphere [e.g. 53, 45]. Figure 10 shows that under these conditions and near the top level of the TIE-GCM (i.e. roughly 500–700 km, depending on solar flux), helium mass mixing ratios exceed 0.8 during solar maximum conditions and 0.9 during solar minimum conditions. Had we instead queried MSIS using the geometric heights calculated by TIE-GCM as our vertical coordinate, values just below 0.5 would have been obtained. As will be shown in Section 3.3, this discrepancy stems from an underestimation of the geometric height in the upper thermosphere by the original TIE-GCM code due to the neglect of helium. In either case, empirical evidence suggests that helium becomes a major neutral component—and perhaps the dominant component—under certain conditions within the spatial domain of the TIE-GCM. In light of these findings, the remainder of this section covers the expansion of the major neutral species composition equation and other modeled processes from a 3-constituent description [9] to a 4-constituent description in order to account for the significant effects of helium.

The evolution of the major neutral species composition can be expressed using the following vector equation (see the Appendix for derivation and a complete definition of variables):

$$\begin{aligned} \frac{\partial}{\partial t} \Psi = & -e^z \tau^{-1} \frac{\partial}{\partial z} \left[\frac{\bar{m}}{m_{N_2}} \left(\frac{T_{00}}{T} \right)^{0.25} \alpha^{-1} \mathbf{L} \Psi \right] + e^z \frac{\partial}{\partial z} \left[e^{-z} K_E(z) \left(\frac{\partial}{\partial z} + \frac{1}{\bar{m}} \frac{\partial \bar{m}}{\partial z} \right) \Psi \right] \\ & - (\mathbf{V} \cdot \nabla \Psi + \omega \frac{\partial}{\partial z} \Psi) + \mathbf{s} \end{aligned} \quad (7)$$

The meanings of several variables have been modified from those originally intended by *Dickinson et al.* [9]. Ψ is now the vector of mass mixing ratios for O_2 , O , and He , while the mass mixing ratio of the remaining major constituent N_2 is specified by $\psi_{N_2} = 1 - \psi_{\text{O}_2} - \psi_{\text{O}} - \psi_{\text{He}}$. Molecular and thermal diffusion are accounted for by the first term on the right side of Eq. (7), eddy diffusion by the second, horizontal and vertical advection by the third, and chemical sources and sinks by the fourth.

\mathbf{L} is a diagonal matrix operator with elements:

$$L_{ii} = \frac{\partial}{\partial z} - \left(1 - \frac{m_i}{\bar{m}} - \frac{1}{\bar{m}} \frac{\partial \bar{m}}{\partial z} - \frac{\alpha_{Ti}}{T} \frac{\partial T}{\partial z} \right) \quad (8)$$

which have been expanded to describe thermal diffusion, a phenomenon which becomes important for species such as helium whose masses are quite different from the mean mass. We use a simplified formulation of thermal diffusion that is analogous to its appearance in the binary diffusion equations, after *Colegrove et al.* [5]. In this treatment, a constant value of $\alpha_{\text{He}} = -0.38$ is used. While this value is characteristic of small concentrations of helium diffusing through molecular nitrogen, this assumption is reasonably accurate at altitudes where significant temperature gradients exist (i.e. below ~ 200 km) [1].

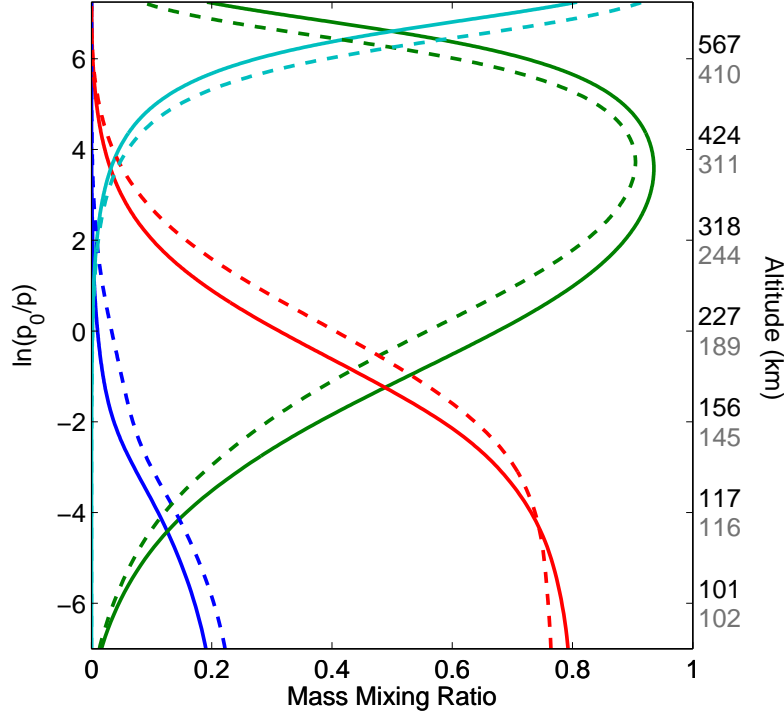


Figure 10: Mass mixing ratio vertical profile . MSIS mass mixing ratios for O₂ (blue), O (green), N₂ (red), and He (cyan) calculated on the vertical log-pressure scale in the vicinity of the winter helium bulge for solar maximum (solid lines/black altitude labels, 21 Dec., 2000) and minimum (dashed lines/grey altitude labels, 21 Dec., 2008) conditions.

The normalized molecular diffusion matrix, α , couples the major components to one another. As can be seen in Eqs. (34) and (39) in the appendix, the strength of this coupling depends on the mutual diffusion coefficients. *Dickinson et al.* [9] assumed these coefficients to take the form $D = D_0(T/T_0)^{1.75}(p_0/p)$ for the major species, after *Colegrove et al.* [5]. Accordingly, the elements of α have been normalized by this functional form. Mutual diffusion coefficients between helium and the other three major species take a similar form, yet with exponents, s , that deviate slightly from 1.75, as seen in Table (3.2.2). These differences have been accounted for by applying correction factors of the form $(T/T_0)^{1.75-s}$ to the appropriate terms within the diffusion matrix α . In the absence of these corrections, the coefficient describing the mutual diffusion between helium and atomic oxygen would remain reasonably accurate, yet those describing the interaction of helium with molecular species would be approximately 5% low.

The chemical source and sink matrix, s , also serves to couple the major species to one another. In the case of helium, however, all chemical and photochemical rates have been set to zero, consistent with our assumption of inertness. Therefore, our current model implementation is appropriate for the study of the dynamical behavior of helium as an ideal inert tracer.

The neutral thermodynamic properties of specific heat, c_p , molecular viscosity, k_m , and conductivity, k_t , have been augmented to include the effects of helium. The following equations are now used [1]:

Table 1: Mutual diffusion coefficients for helium with major species¹.

$i-j$	a	s
He–O ₂	0.649	1.710
He–O	0.866	1.749
He–N ₂	0.622	1.718

¹ $D_{ij} = a (T/T_{00})^s (p_{00}/p)$, $T_{00}=273$ K, $p_{00}=10^6$ g/(cm · s²) [cf. 1, table 15.1].

$$c_p = \frac{R}{2n} \left(\frac{7}{32} n_{O_2} + \frac{5}{16} n_O + \frac{7}{28} n_{N_2} + \frac{5}{4} n_{He} \right) \text{ erg} \cdot \text{g}^{-1} \text{K}^{-1} \quad (9)$$

$$k_m = \frac{10^{-6} T^{0.69}}{n} (4.03 n_{O_2} + 3.90 n_O + 3.43 n_{N_2} + 3.84 n_{He}) \text{ g} \cdot \text{cm}^{-1} \text{s}^{-1} \quad (10)$$

$$k_t = \frac{T^{0.69}}{n} (56.0(n_{O_2} + n_{N_2}) + 75.9 n_O + 299.0 n_{He}) \text{ erg} \cdot \text{cm}^{-1} \text{s}^{-1} \text{K}^{-1} \quad (11)$$

where R is the universal gas constant, T is the neutral temperature in units of Kelvin, n_i refers to the number density of the subscripted species, and n is the total number density.

Additionally, in the description of ambipolar diffusion, the collision frequency, ν_{in} , has been updated to account for nonresonant collisions between O^+ ions and neutral helium atoms. The following form is adopted [64]:

$$\nu_{in} = 1 \times 10^{-10} (6.64 n_{O_2} + 0.367 n_O \sqrt{T_r} (1 - 0.064 \log_{10} T_r) + 6.82 n_{N_2} + 1.32 n_{He}) \quad (12)$$

where $T_r = (T_i + T)/2$ is the average of the ion and neutral temperatures. T_r , ν_{in} and n_i are in units of Kelvin, s⁻¹ and cm⁻³, respectively.

3.2.3 Boundary Conditions

At the lower boundary of the model, atomic and molecular oxygen adhere to the conditions specified in the original TIE-GCM implementation, namely, that the peak of the atomic oxygen density profile lies at the lower boundary and the total amount of oxygen atoms remains constant making up 23.4% of the total mass. In addition, we specify a constant lower boundary mass mixing ratio for helium of 1.154×10^{-6} . In terms of mass mixing ratios, these considerations take the following form: (1) $\partial\psi_O/\partial z = \psi_O$, and (2) $\psi_{O_2} + \psi_O = 0.234$, and (3) $\psi_{He} = 1.154 \times 10^{-6}$.

Near the upper boundary of the model, either atomic oxygen or helium typically dominates the composition, depending on season, solar flux, and location. The original upper boundary of the TIE-GCM is specified by diffusive equilibrium for neutral species, i.e. $L\Psi = 0$. However, the large thermal velocity of helium warrants proper consideration of helium transport processes occurring above the upper boundary in a near-collisionless environment. While the classical thermal escape flux of helium is several orders of magnitude too low to have a noticeable effect on the global helium content, the lateral transport of helium atoms with ballistic trajectories is significant. *Hodges and Johnson* [21] and *Hodges* [20] outline a method for approximating this type of transport, expressing it as a vertical outward particle flux:

$$\Phi = -\nabla^2 (n \bar{v} H^2 P) \quad (13)$$

where ∇^2 is the surface Laplacian. The variables Φ , n , \bar{v} , and H are respectively the vertical particle flux, number density, mean thermal speed, and scale height, all specific to helium. P , a dimensionless factor arising from integration over Maxwellian distributions, has a weak dependence on neutral temperature that can be adequately approximated by [21]:

$$P \approx \left(1 + \frac{T}{3300}\right) \quad (14)$$

for neutral temperature, T , in units of Kelvin. Inherent in these equations is the assumption that collisions do not occur above the upper boundary of the TIE-GCM.

In practice, this vertical flux can be prescribed at the upper boundary of the model as a diffusive flow. The following vector equation describing molecular diffusion is used:

$$\mathbf{w}_D = \tau^{-1} \left(\frac{T_{00}}{T} \right)^{0.25} \frac{p_0 \bar{m}}{g m_{N_2}} \boldsymbol{\alpha}^{-1} \mathbf{L} \boldsymbol{\Psi} \quad (15)$$

where \mathbf{w}_D is the (3×1) vector of vertical diffusive mass flow rates for O_2 , O , and He , respectively. From the derivation of Eq. (15) in the appendix (see Eq. 41), it follows that the diffusive mass fluxes of all neutral species sum to zero. Because molecular oxygen and nitrogen densities are small near the upper boundary, we enforce this constraint by assuming that any outward (inward) mass flux of helium is balanced by an inward (outward) flux of atomic oxygen. Any error that this assumption incurs in the solution of atomic oxygen concentration is diminished by the factor of 4 difference between the mass of oxygen and helium atoms.

In the current implementation of our model, the argument of the Laplacian from Eq. (13) is transformed into a non-aliasing spherical harmonic expansion. This is completed using the technique of *Swarztrauber* [73], modified to accommodate the TIE-GCM's horizontal grid which is offset from the pole by a half-grid increment. The flux, Φ , is then calculated using the well-known eigenfunction/eigenvalue relation:

$$\nabla^2 Y_n^m = -\frac{n(n+1)}{R^2} Y_n^m \quad (16)$$

where Y_n^m refers to the spherical harmonic function of degree n and order m , and R is a characteristic radius of the exobase. In the current implementation, R has been set to the radius of the Earth for consistency with calculations of other horizontal derivatives within the TIE-GCM. The mass flux required by the left-hand-side of Eq. (15) can then be obtained by transforming back to the spherical grid and multiplying the obtained particle flux by the molecular mass of helium. The advantage of using this technique in place of finite differences for calculating the Laplacian is that waves are resolved uniformly over the Earth. Therefore, the growth of numerical instabilities can be controlled by truncating the expansion prior to transforming back to the spherical grid. We note that the degree of truncation required is sensitive to the level of the upper boundary, the grid-size, and the time step. When using the default $5^\circ \times 5^\circ \times H/2$ spatial grid with upper boundary of $z = +7$ and a 120 second time step, we have found that a triangular truncation of degrees higher than 4 is sufficient to limit the growth of numerical instabilities without severely

compromising the accuracy of the exospheric transport model. The adjustment of this truncation parameter, as well as the characteristic exobase radius, R , are left as tasks for future work.

3.2.4 Software Development

Table 1 gives an overview of TIE-GCM-He version evolution and capabilities.

Table 2: Software development history.

Version/Date	Description of Commit
V1.0 12/06/2012	First version to run with 4 major species O ₂ , O, He, N ₂ , still need to make several changes throughout the model. Any instance of N ₂ or mbar being calculated, need to be changed from 1-o ₂ -o ₁ to 1-o ₂ -o ₁ -he and from 1/(o ₂ /mo ₂ +o ₁ /mo ₁ +n ₂ /mn ₂) to 1/(o ₂ /mo ₂ +o ₁ /mo ₁ +he/mhe+n ₂ /mn ₂).
V1.1 12/11/2012	Updated addiag.F so that Helium is taken into account when mbar, xnmbarm, xnmbari, xnmbarm, DEN, Z, ZG and others are calculated. Changed small value threshold from 1e-6 to 1e-9 for Helium only. Changed the section that insures non-negative n ₂ values: previously the denominator differed when normalizing o ₁ and o ₂ (this seems to be a bug in the original code).
V1.2 12/12/2012	Added thermal diffusion to comp.F for Helium.
V1.3 12/13/2012	Updated cpktkm.F to take Helium into account when calculating specific heat, molecular diffusion of heat (conduction) and molecular viscosity.
V1.4 06/03/2013	Modified the calculation of local variable xnmbarm in comp_o2o.F to account for Helium; the variable is used to calculate prod/loss rates of o ₂ , o ₁ , and he. Floor(sflux) in qrj.F is changed from 80% to 10% of sfmin, this only comes into play during very low solar flux; per Stan Solomons instruction (see email dated 17-Jan-2013). Made co _{2u} variable within subroutine newton time-varying to capture the change in CO ₂ over time in order to make a run that is consistent with Solomon et al. 2011.
V1.5 07/01/2013	Specified a diffusive flux upper boundary condition in the major species equation describing the lateral exospheric transport of helium occurring above the model upper boundary. This required substantial modification of comp.F, as well as a very slight modification of cons.F, cons.variableCO ₂ .F, and dynamics.F.
V1.6 08/19/2013	This is the last internal AFRL version separate from NCAR/HAO resulting from meeting with NCAR (S. Solomon, W. Wang, and B. Foster). Identified several instances of (1-o ₂ -o ₁), and implemented a new variable n ₂ =(1-o ₂ -o ₁ -he) to fix all occurrences throughout model. Reestablished MPI functionality. Inducted model into the NCAR software repository as a branch of TIE-GCM to facilitate future model development.
	NCAR/HAOs subversion revision numbers are adopted hereafter
r966 08/19/2013	tiegcm/branches/tiegcm_he: - Merge this branch from its origin at tag tiegcm1.94.2 with the current trunk (r950).
r967 08/20/2013	tiegcm/branches/tiegcm_he: - Added N ₂ as a new 3d field in fields.F (defined in addiag.F). - Replaced code using (1.-o ₂ -o ₁ -he) with the new N ₂ field (addiag.F, comp.F, comp_o2o.F, and cpktkm.F). N ₂ is passed to these routines via the calls in advance and dynamics. - At this point, the code produces identical results as MPI runs from the previous commit, and is therefore still very close to Eric's original non-mpi code. - Next, I will replace code using (1.-o ₂ -o ₁) with n ₂ (which is now 1.-o ₂ -o ₁ -he), so after that is committed, results will be different than Eric's original code. This occurs in several routines (chapman, comp_n4s, comp_no, dt, duv, elden, lamdas, minor, etc)
r968 08/21/2013	tiegcm/branches/tiegcm_he: - Replaced all occurrences of 1.-o ₂ -o ₁ with the new n ₂ 3d array, which is now 1-o ₂ -o ₁ -he. This means the results will differ from the previous commit, and Eric's original non-mpi code. Results are presumably more accurate because now helium is included in N ₂ . - Added new N ₂ diagnostic in diags.F. mkdiag_N2 is called from comp.F to save updated N ₂ to secondary histories. Now users can add 'N2' to namelist SECFLDS without having to call addfld. - Note helium was not included in the calculation of the bottom interface level of n ₂ (n2i(1,...)) in qinite.F and qrj.F. For now, I am using n2i(lev0,...) = 1.-o ₂ i(lev0,...)-o ₁ i(lev0,...) because helium is negligible at this bottom boundary level. Search on "btf tiegcm_he" to find this in the source code.
r973 08/28/2013	tiegcm/branches/tiegcm_he: - The problem described in the previous revision (r969) was a result of a misplaced parenthesis in rrk. This commit fixes that problem, and also adds He/O+ collision frequency provided by Wenbin.

r1012 02/03/2014	<p>tiegcm/branches/tiegcm_he:</p> <ul style="list-style-type: none"> - Update this branch from the trunk, including all changes to the trunk since this branch was started (r964). This was done w/ the following merge command, executed from an up-to-date working copy of the branch: <code>svn merge -r964:HEAD \$SVN/tiegcm/trunk</code>. There were no conflicts. This is in preparation for merging the helium branch to the trunk.
r1013 02/03/2014	<p>tiegcm/trunk:</p> <ul style="list-style-type: none"> - Merge the tiegcm branch tiegcm_he to the trunk. This was done with the following command, executed from an up-to-date working copy of the trunk: <code>svn merge \$SVN/tiegcm/trunk \$SVN/tiegcm/branches/tiegcm_he</code> - There were no conflicts with this merge, which follows a recent merge to update the helium branch from the trunk (see -r1012). - This adds helium 'HE' as a prognostic in the model, so it is included in primary histories, along with helium at the previous timestep 'HE_NM'. The code to solve for helium was provided by Eric Sutton, and parallelized by myself. See especially new source files <code>laplacian.F</code>, and <code>sh_coef.F</code>. All calculations of neutral density, and N2 were modified appropriately. N2 was added as a 3d diagnostic. - Many of Eric's comments ("Added by EKS", "Modified by EKS", etc) were removed for this commit to the trunk (all of them were retained in the tiegcm_he branch). - For more details regarding the addition of helium in the model, please see the svn commit log for <code>\$SVN/tiegcm/branches/tiegcm_he</code>.
r1047 05/08/2014	<p>tiegcm/trunk:</p> <ul style="list-style-type: none"> - Helium at 2.5-degree resolution is now working, thanks to Eric Sutton for providing laplacian coefficients for this resolution. See new source files <code>he_coef0.dres.F</code> (lpmn), and <code>he_coef1.dres.F</code> (zmn). Also changed the name of coefficients file for 5-deg resolution from <code>sh_coef.F</code> to <code>he_coefs_sres.F</code>. These three files are modules with data statements dependent on resolution as determined by cpp #if conditionals. They are use-associated by <code>laplacian.F</code>. - Set <code>calc_helium</code> namelist flag to 1 for both resolution default namelist input files in the scripts directory (see r1042). Removed trap to shutdown if <code>calc_helium=1</code> at 2.5-degree resolution.
r1061 06/23/2014	<p>tiegcm/trunk:</p> <ul style="list-style-type: none"> - Set HE lower boundary (mmr) <code>pshelb = 0.1154E-5</code> (see <code>lbc.F</code>) (in <code>timegcm</code>, <code>pshelb=7.18e-7</code>). <code>Pshelb</code> is used in subs <code>bndef</code> and <code>bndcmp</code> (<code>lbc.F</code>) to set the lower boundary (gg, fb, etc). If a history is read that does NOT have helium, then the 3d (global and vertical) HE and HE_NM are initialized to <code>pshelb</code> (see <code>rdsources.F</code>). This helps "prime" helium on its approach to steady state without a starting field from the history. Continuation runs of course read helium from the given history from which to continue. - A 5-deg run of tiegcm from March equinox solar minimum conditions, showed that it can take 80 days for helium to reach approximate steady state, starting from global <code>pshelb</code>. <p>I will be making a similar commit in the timegcm trunk.</p>
r1060 06/16/2014	<p>tiegcm/trunk:</p> <ul style="list-style-type: none"> - Pass helium to minor through <code>comp_no</code> and <code>comp_n4s</code>, so it can be included in <code>xmbari</code>, <code>xmbar.kh</code>, etc. See <code>minor.F</code>. - To be completely correct and consistent, we will also have to add <code>pshe</code>, <code>dhedz</code> (analogous to <code>pso2</code>, <code>do2dz</code>, etc), and make <code>alfa</code> 3x3 instead of 2x2 so minor species diffusion through the major species will include helium (see <code>ex(k,i)</code>). See "btf 6/16/14" comment in <code>minor.F</code>. I am working with Wenbin on this.
r1074 08/14/2014	<p>tiegcm/trunk:</p> <ul style="list-style-type: none"> - Add argon as a minor species. This is similar to the r1069 commit which added argon to the timegcm trunk. New source file <code>comp_ar.F</code>. - As in <code>timegcm</code>, global mean column values from <code>glbmean</code> model are used to initialize argon when it is not available on the source history. - Note that tiegcm does not calculate horizontal diffusion for minor species, like <code>timegcm</code> does. - Test runs have been made at both 5.0-deg and 2.5-deg resolutions, but further testing and validation of argon should be done with this code before the next major release (v2.0).

r1119 01/21/2015	<p>tiegcm/trunk (helium):</p> <ul style="list-style-type: none"> - Modifications to helium calculation recommended by Eric Sutton, during his visit to hao this week (see also email correspondence in Nov, 2014): - Deleted data array lpmn which contained $(m^2/\sin(\theta) - n(n+1)) \cdot \text{pmn}$. The $m^2/\sin(\theta)$ term is not needed. Therefore, I replaced lpmn with pmn (the normalized associated legendre polynomials) and added the latitude-independent term $-n(n+1)$ to the synthesis loop within laplacian.F. (src/coefs.sres.F and src/coef0.dres.F) (makes this commit a large change set) - Added compiler (preprocessor) #IF statement and parameter 'truncdeg' to define the degree of truncation for the spectral approximation, which depends on grid resolution and upper boundary pressure level. Set truncdeg=4 for default (5-deg) resolution, and truncdeg=8 for double (2.5-deg) resolution. - Minor updates to comments in laplacian.F, comp.F, he_coefs.sres.F, and he_coef0.dres.F. - The 'Fit' and 'Synthesis' sections of laplacian.F each now contain commented loops (just after the main loops) that are helpful when debugging various levels of truncation and testing for stability. - Removed unneeded z argument in comp.F (and removed it from the call to comp in dynamics.F). - Left addfld calls for FLX_HE and FLX_ARG uncommented in comp.F (after call to laplacian).
r1125 01/28/2015	<p>tiegcm/trunk:</p> <ul style="list-style-type: none"> - The following comments are from Eric Sutton (see correspondence 1/22/15): - A temperature dependent variation was applied to the coefficients describing diffusion of helium with the other major species (comp.F). In previous versions, the temperature and pressure dependence of diffusion coefficients were normalized by assuming a variation of the form $(p_0/p) \cdot (T/T_0)^{1.75}$. In the case of helium, the exponent 1.75 is not realistic, requiring a correction factor of $(T/T_0)^{(1.75-s)}$, where s is the appropriate exponent, to be multiplied to the normalized diffusion coefficients (ϕ's) describing He-O₂, He-O, and He-N₂ diffusion. The correction factor is generally on the order of 5%.

3.3 Results and Discussion

In this section, we present the salient features of the new model. While many simulations were necessary in order to distill our description of these features with respect to season, local time, latitude, external forcing parameters, and boundary conditions, only a small subset of simulations are presented. These were created using the model settings and inputs described in Section 3.2.1, and are specific to the prevailing solar and geophysical conditions of 2008. Section 3.5 includes additional plots to aid in visualization, specifically regarding the sensitivity of the helium distribution to external forcing and boundary conditions.

Figure 11 shows helium densities at 250 km altitude simulated by the TIE-GCM during each of the four seasons of 2008. The winter helium bulge phenomenon is clearly present at both solstices. During the equinoxes, the helium bulge undergoes a migration from the spring hemisphere to the fall. Along the way, helium levels are briefly enhanced at low latitudes with a strong preference for early morning local times, with the full transition taking approximately 1–2 months. At winter solstice, a similar preference for early morning is tempered by an aversion to the auroral zones, where pockets of divergence and upwelling lead to localized helium depletions. This balance manifests as a diurnal modulation of the winter helium bulge in latitude and local time. Symptoms of this behavior can be seen in the the upper right panel of Figure 11, where the southern hemisphere winter peak occurs around 16:00 LT. For reference, the geomagnetic poles are located at 82.4°N/18:30 LT and 74.5°S/8:20 LT in these plots.

The high-latitude helium distribution is further complicated by short-scale variations in geomagnetic heating. In general, helium densities tend to increase at low latitudes during periods of geomagnetic activity. The opposite is true in the polar region during solstice, as the high-latitude upwelling and divergence resulting from geomagnetic activity tend to lift heavy constituents while dispersing helium over a larger horizontal expanse.

The distribution of helium is highly sensitive to geomagnetic activity, the effects of which can

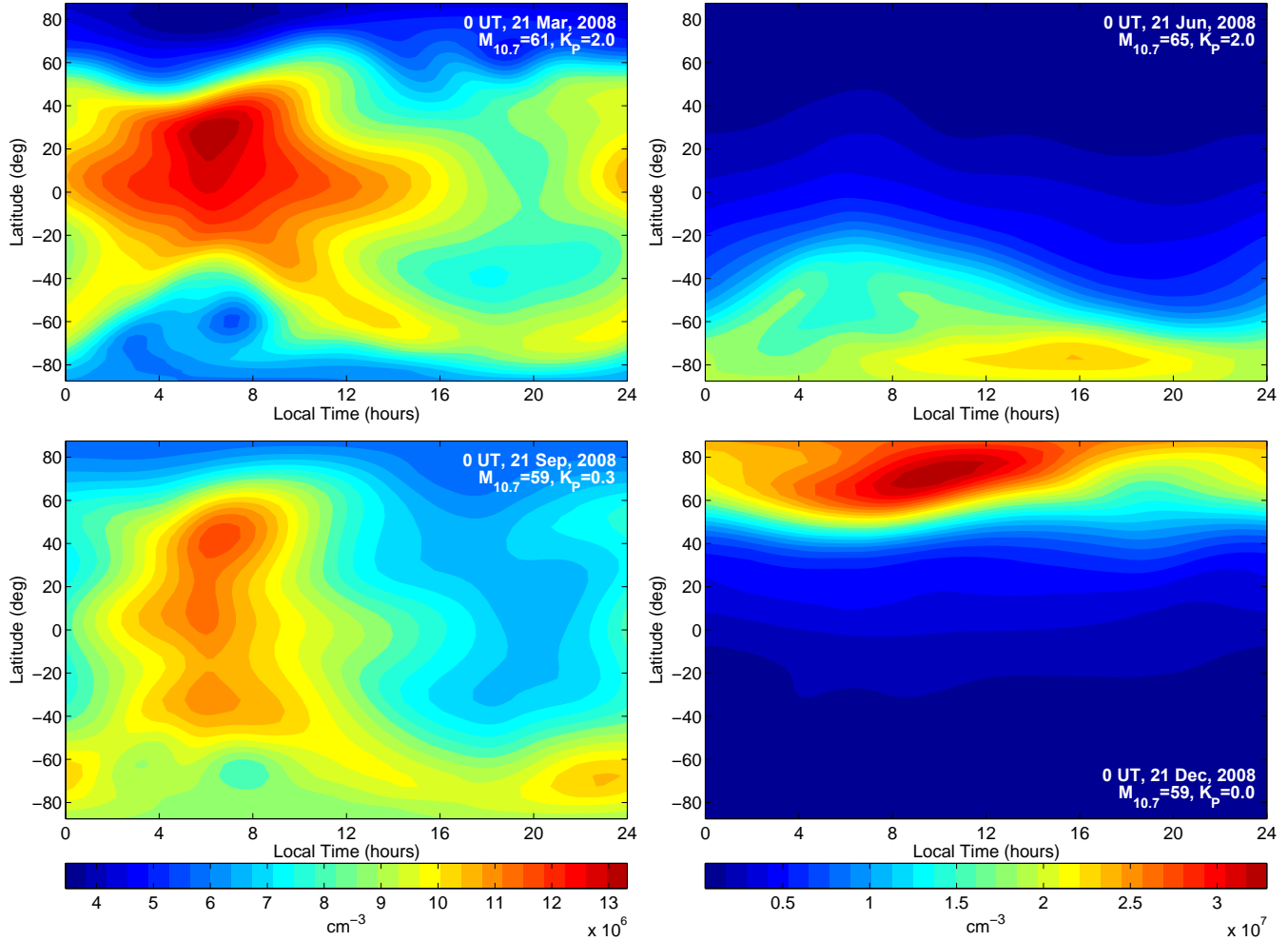


Figure 11: Helium concentration (TIE-GCM). Global distribution of helium number densities at 250 km altitude during each season for solar minimum conditions (2008), as calculated by TIE-GCM. Equinox plots (left) share a common color scale, as do solstice plots (right).

be seen in the contrasting equinoctial helium distributions of Figure 11. The March equinox consists of enhanced low and middle latitude helium densities accompanied by depletions closer to the poles, all associated with a slight elevation in the level of geomagnetic activity over the previous 3-hour period ($K_P=2.0$) relative to the September equinox ($K_P=0.3$). The same argument can be applied to the solstice plots of Figure 11, wherein the slightly disturbed ($K_P=2.0$) June solstice helium distribution is shifted away from the winter pole in comparison to the undisturbed ($K_P=0.0$) December solstice. The helium distribution is most certainly influenced by the time history of geomagnetic activity over the previous ~ 24 hours or more. As such, an index describing the level of geomagnetic activity over a 3-hour interval may not generally be a reliable indicator. However, in all four of the cases presented the 3-hour K_P index is fairly representative of the levels of geomagnetic activity during the previous 24-hour period. The solstice comparison is less straightforward than for equinox due to several additional complications. One such complication is that the location of maximum helium concentration is more sensitive during solstice to

the location of the geomagnetic poles. The solstice comparisons also suffer from slightly differing amounts of solar flux. The Supporting Information provides additional figures emphasizing the sensitivity of the helium distribution throughout the year to variations in geomagnetic activity, solar flux, and forcing of the lower boundary by migrating tides.

As a basis for comparison, Figure 12 shows helium densities at 250 km altitude as calculated by the MSIS model. Many of the salient features are qualitatively similar to those of the TIE-GCM, with respect to seasonal, latitudinal, and local time characteristics. MSIS helium distributions clearly exhibit the same strong preference for the winter polar regions during solstice, and for the low-latitude, early local time sectors during equinox. Likewise, a similar sensitivity to geomagnetic effects is evident within MSIS. Notice, however, that the color scales differ between Figures 11 and 12 in order to show behavior over the full range of each model. At 250 km, the TIE-GCM typically underestimates the magnitude of the MSIS helium bulge by approximately 20% during solstice, while overestimating it by 5% during equinox. This agreement is reasonable, considering that no adjustments have been made to the TIE-GCM in an effort to improve model agreement.

Likewise, the MSIS model estimated and applied correction factors for the underlying mass spectrometer data [13], which could further limit the absolute accuracy of such model comparisons. In certain cases, there are discrepancies in the location and shape of the helium bulge between models. For instance, the location of maximum helium concentration during the June solstice is out of phase by about 8 hours in local time between the two models. While the MSIS helium distribution is prescribed, to a certain extent, by a trade-off between the data sparsity of its underlying historical data set and the complexity of its basis functions, further investigation is needed before attributing any discrepancies to the shortcomings of either model.

Figure 13 shows the magnitude of the helium bulge ratio as a function of height, during solar minimum solstice conditions. These profiles were constructed by taking the ratio of maximum-to-minimum helium number densities along each model meridian to roughly approximate the method of calculation used in previous studies. The ratio at each height was then averaged both zonally and over the course of a day; note that no attempt was made to specify the local time sampling of a particular polar-orbiting satellite. The vertical profiles exhibit a quick increase from the lower boundary, giving way to a maximum around 175 km, then decaying slowly with altitude to the upper boundary. This behavior can be explained by the transition from a region below the peak which is dominated by collisions, to a region above the peak where diffusive equilibrium is well established. Below the height of maximum bulge ratio, the summer-to-winter bulk circulation pattern leads to the accumulation of helium in the winter hemisphere. Above this height, however, vertical profiles begin to approximate diffusive equilibrium, causing helium densities in the winter hemisphere to decrease with height at a slightly faster exponential rate than those in the warmer summer hemisphere.

The significant difference between June and December is due to a combination of lower solar flux and geomagnetic activity during the December solstice. Smaller contributions to this difference may arise from seasonal variations such as in the eddy diffusivity. Error bars in Figure 13 show the standard deviation of the helium ratio over the course of a day, giving an indication of the sensitivity to diurnal variations as well as small variations in geomagnetic activity. Below 150 km, smaller standard deviations are seen, indicating that variations in the lower part of the profile take place on longer timescales. Presumably, the lower portion of the profile is more sensitive to season and solar flux than to short-scale geomagnetic activity. Approaching altitudes as

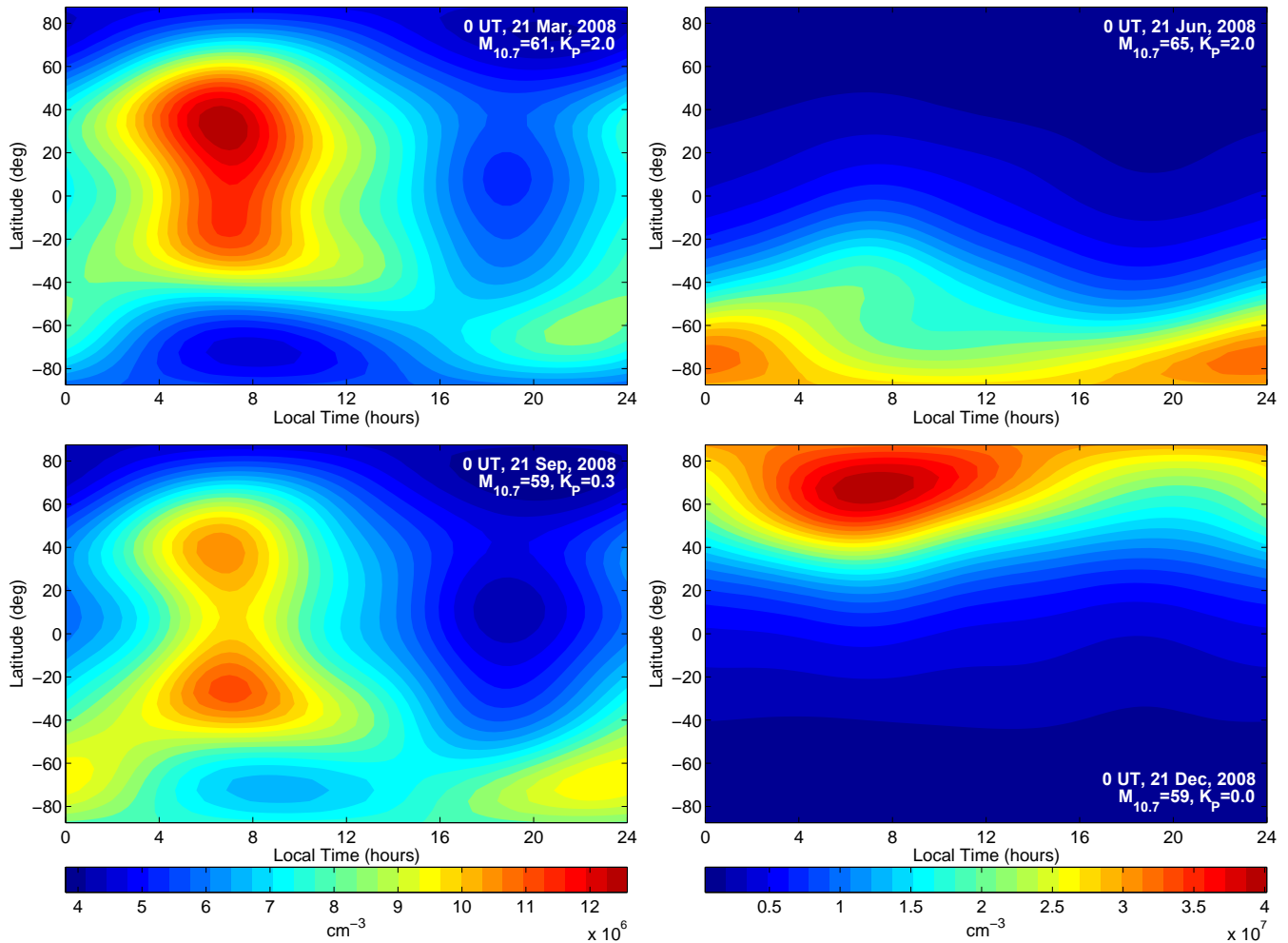


Figure 12: Helium concentration (MSIS). Global distribution of helium number densities at 250 km altitude during each season for solar minimum conditions (2008), as calculated by MSIS. Equinox plots (left) share a common color scale, as do solstice plots (right); these are distinct from the color scales of Figure 11.

low as 100 km, the two profiles begin to converge, suggesting a muted response to geomagnetic activity as well as to seasonal variations.

The addition of helium to the TIE-GCM has several feedback effects on the global structure of the model. Most of these are related to the change in the mean mass, which can become quite small and even approach 4 amu near the top of the model. On levels of constant pressure, such a decrease in the mean mass corresponds directly to a decrease in mass density. At a fixed height, however, this behavior is accompanied by the expansion of the atmosphere according to the ideal gas law, causing levels of constant pressure to move upward. With increasing altitude, the expansion effect begins to dominate the mean-mass effect such that the decay in mass density with height becomes much more gradual when helium is considered. Figure 14 shows the induced increase in mass density at a fixed altitude of 415 km. While the inclusion of helium causes the model's upper boundary to expand considerably higher than 415 km, we chose this

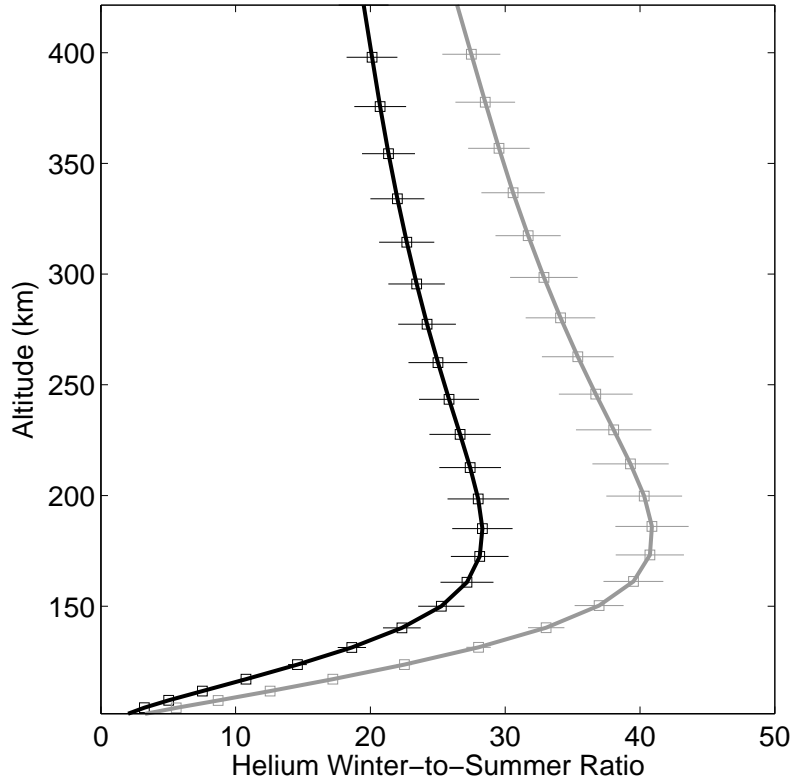


Figure 13: Winter helium bulge ratio. Vertical profile of the winter-to-summer helium bulge ratio during solar minimum June (black, June 21, 2008) and December (grey, Dec. 21, 2008) solstice conditions. The profiles represent the daily average of the ratio of maximum-to-minimum helium number densities taken along each meridian, roughly approximating the sampling of a polar orbiting satellite (see text for a detailed explanation). Error bars indicate the standard deviation of values over the course of a day.

height for our comparison because it was the highest altitude that remained within the vertical domain of the original TIE-GCM simulations during each of the four time periods shown.

The increase in mass density is most noticeable during solstice, where differences of 20-25% can be seen. Both equinox and solstice mass density increases are largest under quiet geomagnetic conditions. While somewhat modest, these percent differences increase with height at an approximate rate of 1% per kilometer near the upper boundary of the TIE-GCM in regions of large helium densities. If the composition of the TIE-GCM is extended vertically into the exosphere under the first-order approximation of diffusive equilibrium, the effects of helium soon become the dominant factor in neutral mass density variations. Under solar minimum conditions, an extension of both models to 500 km results in differences on the order of 50% during equinox and 100-200% during solstice. At 600 km, the solstice differences exceed of an order of magnitude.

Contours in Figure 15 show differences in the height of a log-pressure level near the top of the model induced by the inclusion of helium. Near the winter pole where these height differences maximize, the atmosphere is uplifted by some 50-60 km when compared to an atmosphere simulated without helium. This modification further couples to the horizontal momentum equations

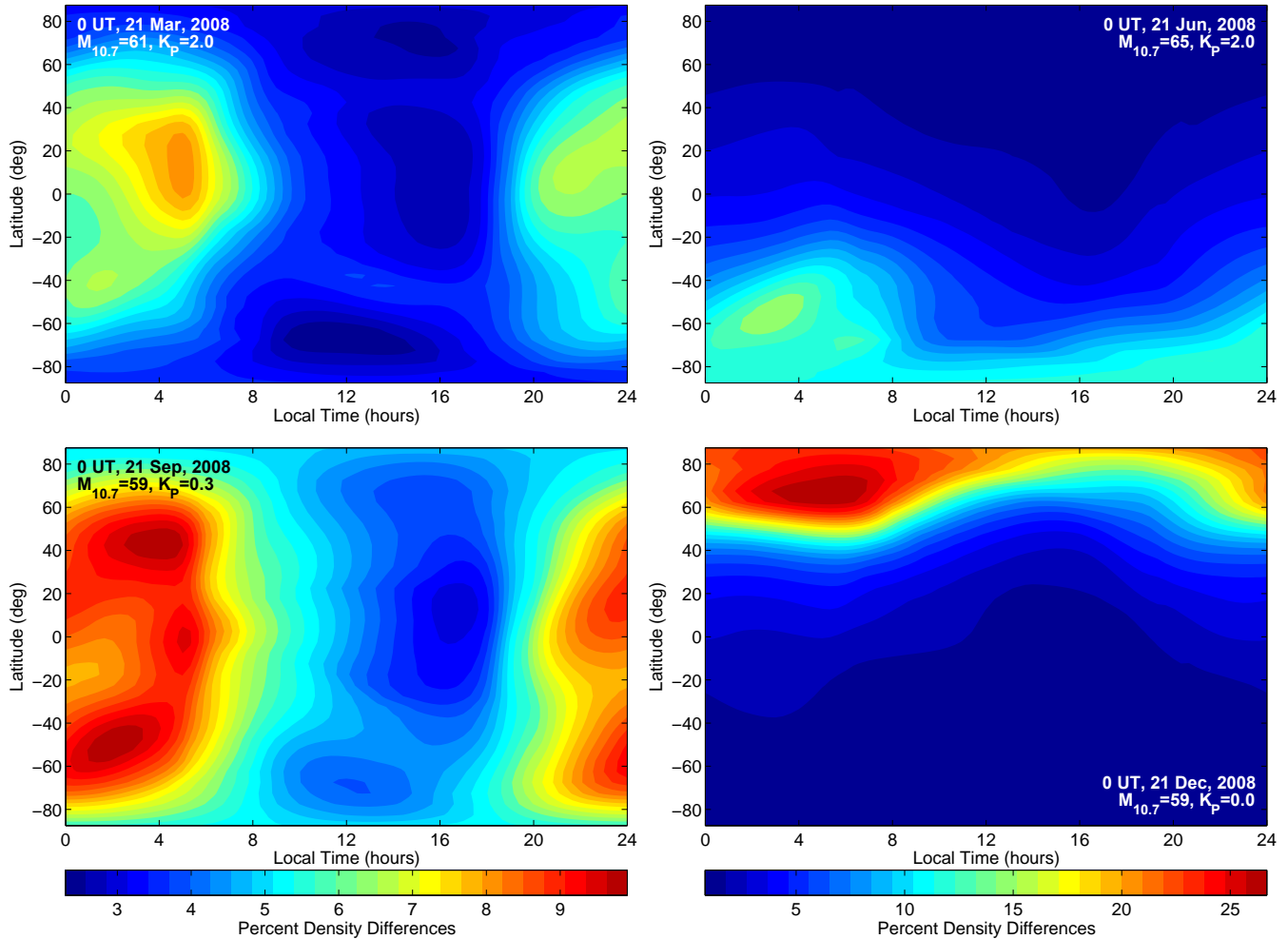


Figure 14: Helium’s impact on mass density. Percent increase in the total mass density at a fixed altitude of 415 km resulting from the inclusion of helium in TIE-GCM during each season for solar minimum conditions (2008). Equinox plots (left) share a common color scale, as do solstice plots (right).

[see 8], increasing horizontal gradients in the geopotential and resulting in a difference wind pattern that flows away from the winter helium bulge, as depicted by the vector arrows of Figure 15. This effect generally becomes noticeable in the upper thermosphere, above 300-400 km, where differences as high as 15-20 m/s can be attained.

3.4 Conclusions

This chapter establishes methods for tracking helium abundance self-consistently throughout the thermosphere. The resulting model simulations qualitatively recreate the expected seasonal/latitudinal behavior while also showing reasonable quantitative agreement with MSIS. Moreover, the model provides winter-to-summer helium ratios that generally agree with solar minimum observations from AE-C [2]. A more rigorous one-to-one comparison between this new model

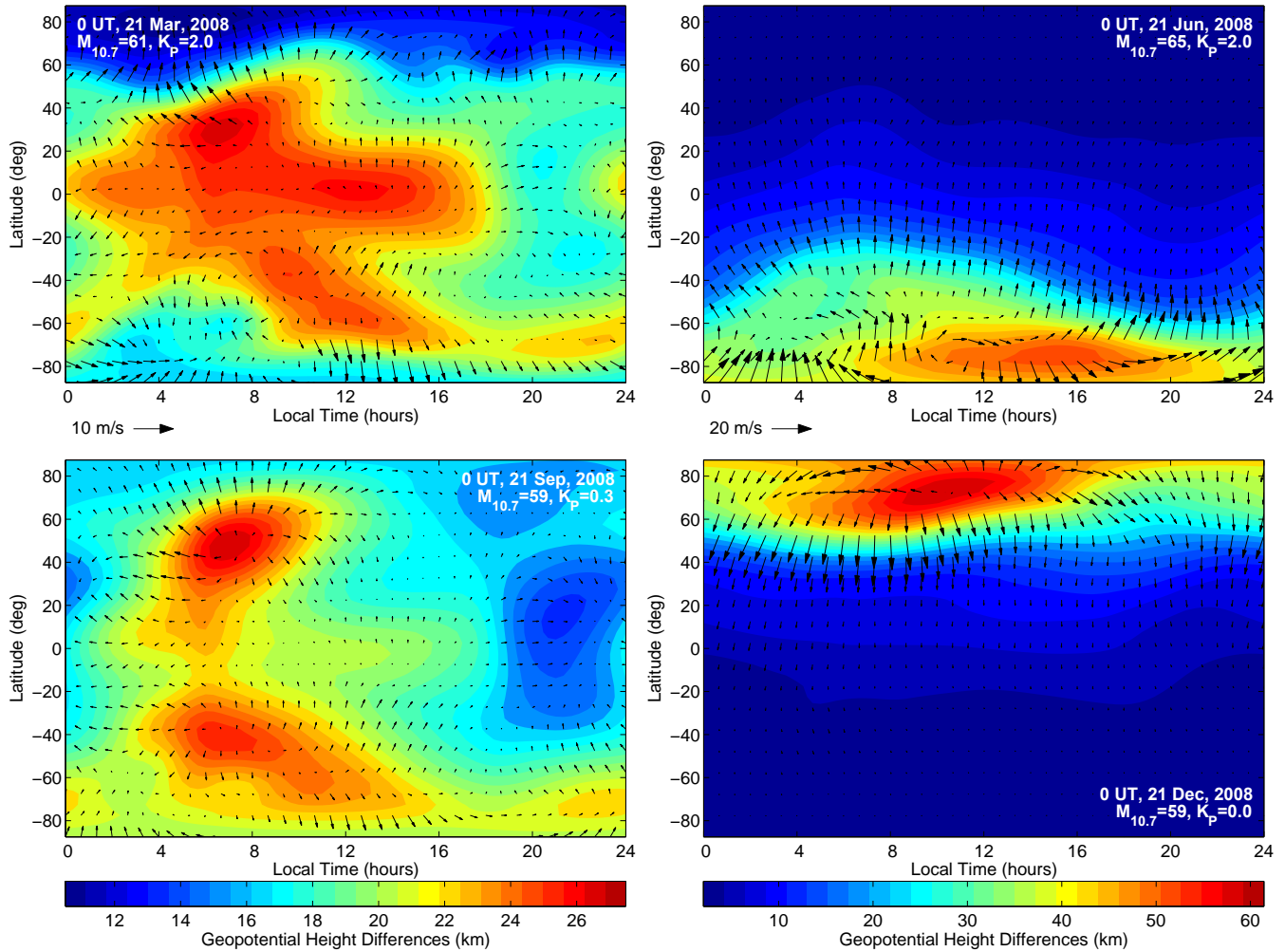


Figure 15: Helium's impact on geopotential height and horizontal winds. Difference in the geopotential height (color contours) and the horizontal wind field (vectors) on a level of constant pressure near the upper model boundary ($z=+6.75$) resulting from the inclusion of helium in TIE-GCM during each season for solar minimum conditions (2008). Equinox plots (left) share common color and vector scales, as do solstice plots (right).

and legacy mass spectrometer measurements is merited; however, this task is left for future work.

Perhaps the most direct application for this new model is related to the increased realism of the neutral mass density vertical profile, and thus the improvement in model performance with respect to satellite drag observations in the upper thermosphere. At a constant height within the model domain, we have shown that including helium in the TIE-GCM causes differences in neutral mass density on the order of 20-30% during solar minimum. The most noticeable differences occur near the upper model boundary during solstice in the winter hemisphere.

Furthermore, helium concentration in the exosphere is highly sensitive to the dynamics of the thermosphere. An appropriate exospheric model could use the TIE-GCM's upper boundary to specify a realistic exobase. Using profiles approximated by diffusive equilibrium above the TIE-GCM's upper boundary, we demonstrated that helium can account for order-of-magnitude differences in neutral density near 600 km and above. These differences, structured in latitude and local time, are strongly modulated by season and geomagnetic activity, lending significant variability to the upper thermosphere and exosphere. This seasonal, latitudinal, and local time helium behavior can be used to inform the structure of semi-empirical model basis functions [e.g. 71]. At a minimum, inferring the amplitude of such basis functions would require sufficient coverage of high-altitude satellite drag measurements, but would be better served by a contemporary set of mass spectrometer measurements.

The value of helium as a tracer of thermospheric dynamics has been known for some time [see 52]. In addition to its ability to diagnose the interplay of circulation and diffusion in the thermosphere, our new model will enable future studies attempting to exploit the sensitivity of the helium distribution to otherwise unobservable system dynamics and inputs. We anticipate that employing helium as a diagnostic tracer—e.g. in order to specify or constrain high-latitude energy inputs, solar-driven circulation pattern strength, and/or sub-grid scale model dynamics—will be beneficial in refining model performance for scientific endeavors as well as operational applications.

3.5 Additional Supporting Information

The supporting information contains several controlled runs illustrating the sensitivity of the helium distribution to geomagnetic activity, solar flux, and migrating tides imposed at the lower boundary.

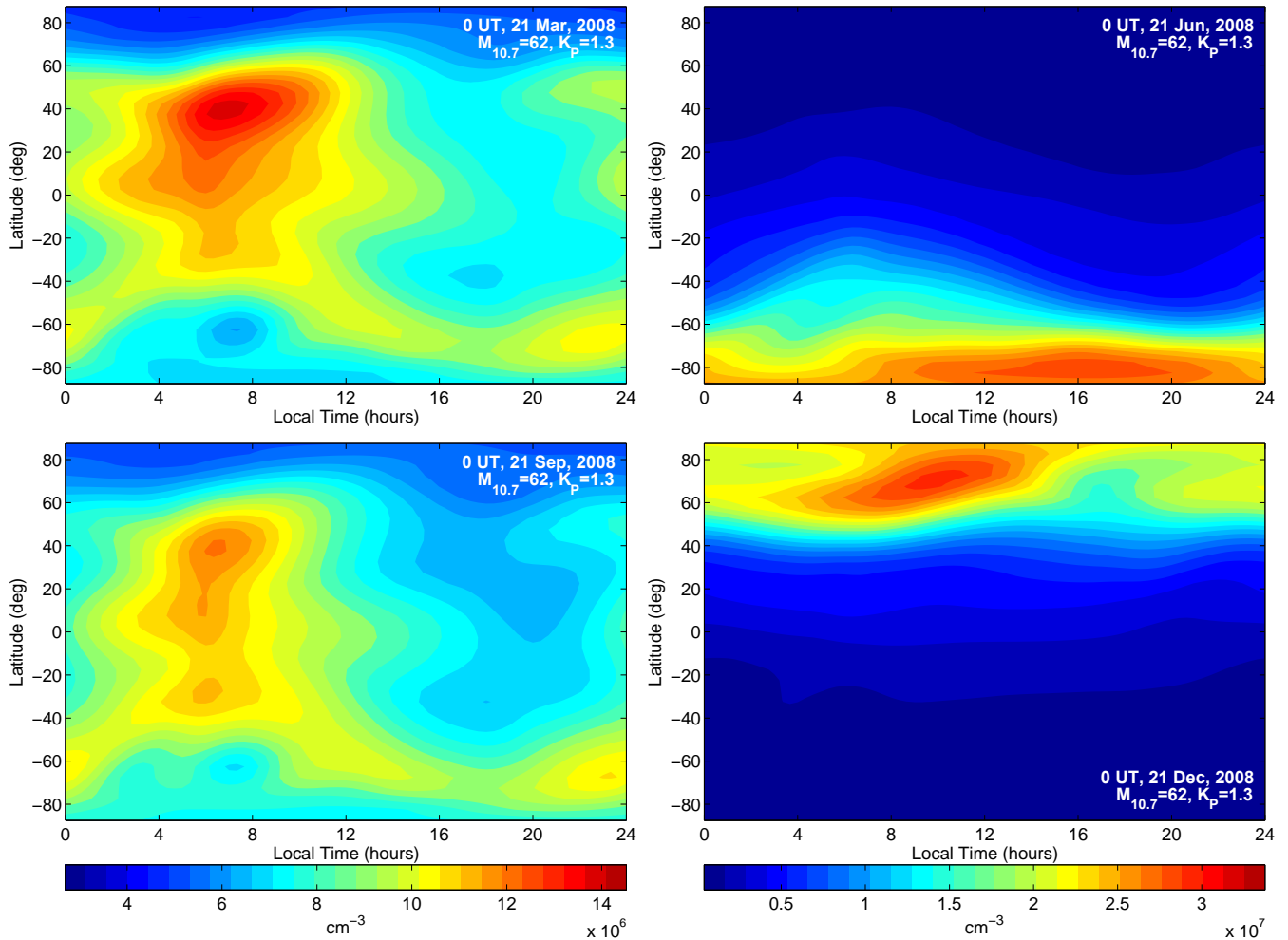


Figure 16: TIE-GCM control run: constant $M_{10.7}$ and K_P . Global distribution of helium number densities at 250 km altitude during each season. Solar and geomagnetic drivers were held constant throughout the year-long simulation at the median values of 2008: $M_{10.7} = 62.0$ and $K_P = 1.3$. Equinox plots (left) share a common color scale, as do solstice plots (right).

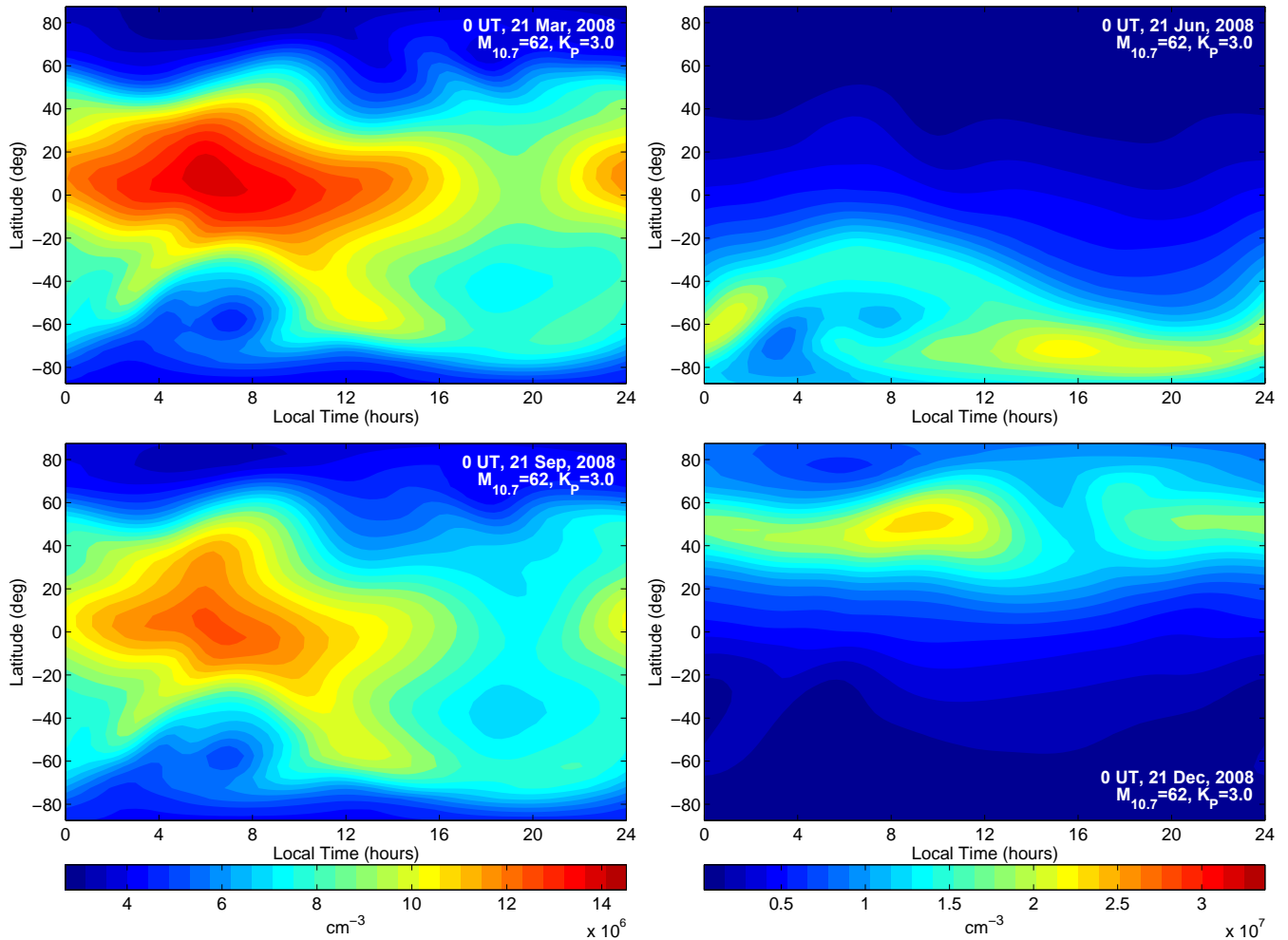


Figure 17: TIE-GCM control run: elevated K_P . Global distribution of helium number densities at 250 km altitude during each season. Solar and geomagnetic drivers were held constant as in Figure 16, but with an elevated geomagnetic index of $K_P = 3.0$. Equinox plots (left) share a common color scale, as do solstice plots (right).

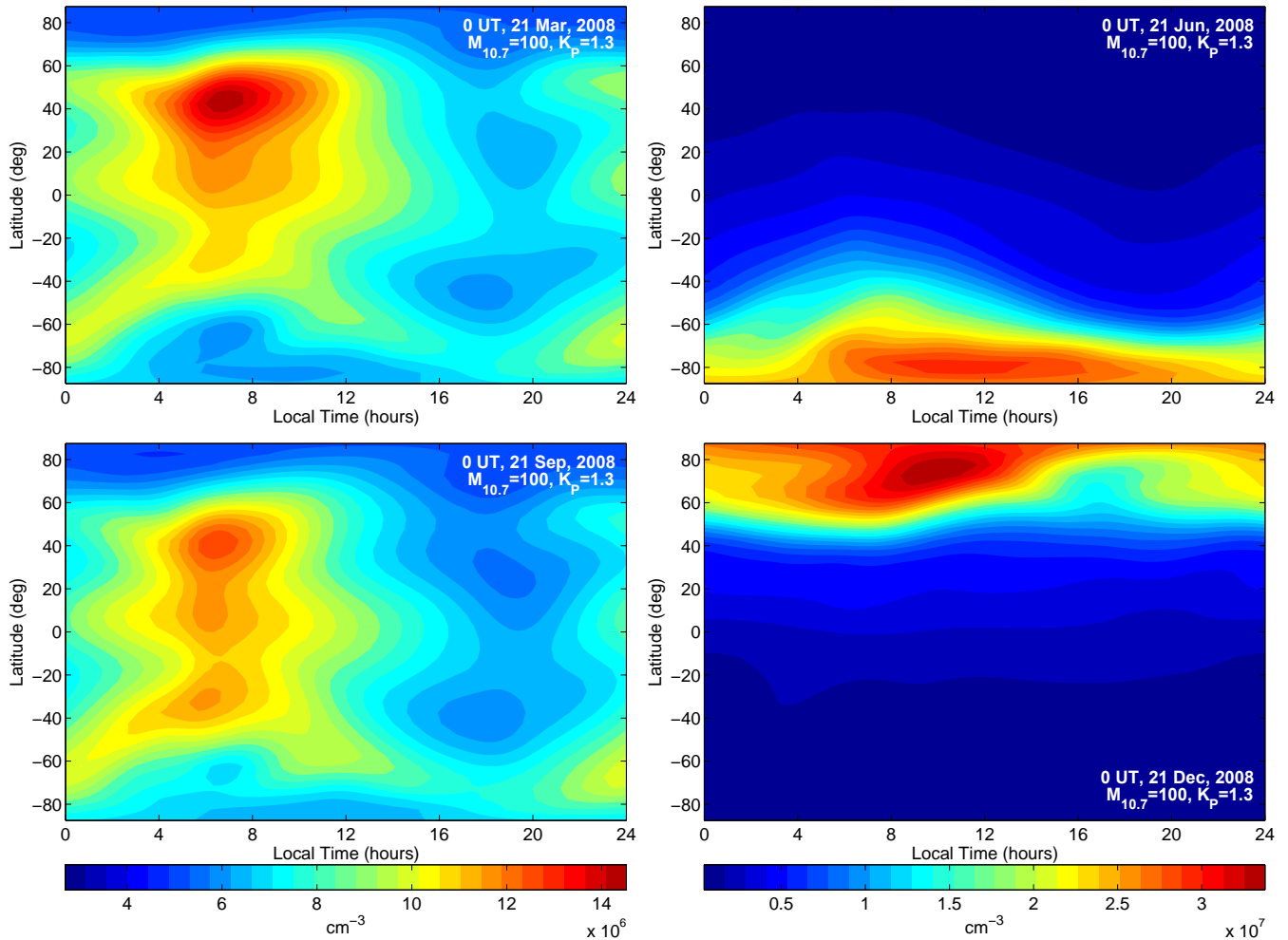


Figure 18: TIE-GCM control run: elevated $M_{10.7}$. Global distribution of helium number densities at 250 km altitude during each season. Solar and geomagnetic drivers were held constant as in Figure 16, but with an elevated solar flux proxy of $M_{10.7} = 100.0$. Equinox plots (left) share a common color scale, as do solstice plots (right).

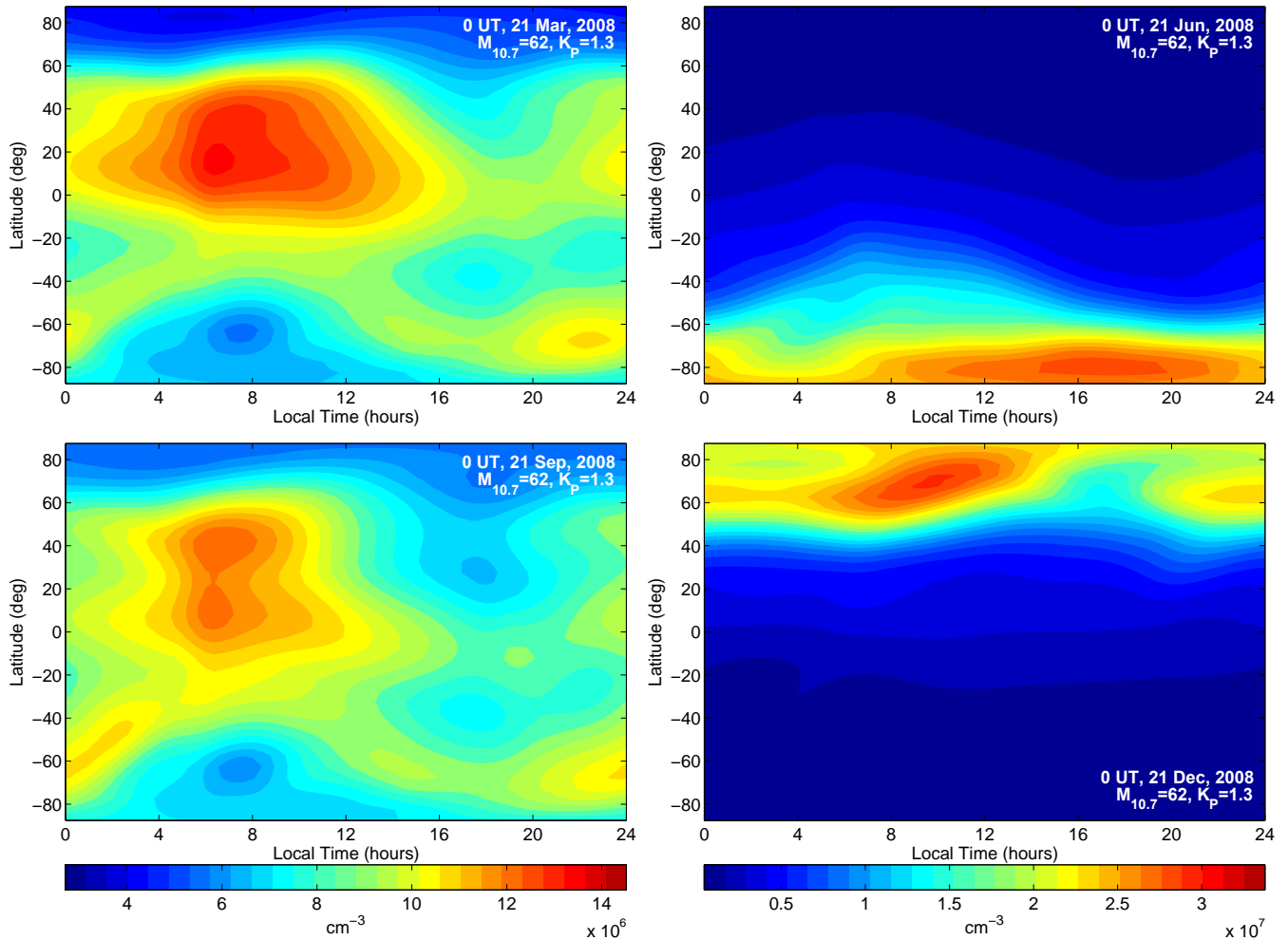


Figure 19: TIE-GCM control run: Tidal Forcing Removed. Global distribution of helium number densities at 250 km altitude during each season. Solar and geomagnetic drivers were held constant as in Figure 16, but with the lower boundary GSWM forcing from migrating tides removed. Equinox plots (left) share a common color scale, as do solstice plots (right).

REFERENCES

- [1] Banks, P. M., and G. Kockarts (1973), *Aeronomy: Part B*, Academic Press.
- [2] Cageao, R. P., and R. B. Kerr (1984), Global distribution of helium in the upper atmosphere during solar minimum, *Planet. Space Sci.*, 32, pp. 1523–1529, doi:10.1016/0032-0633(84)90019-9.
- [3] Chapman, S., and T. G. Cowling (1970), *The Mathematical Theory of Non-Uniform Gases*, 3rd ed., Cambridge: University Press, 1970.
- [4] Colegrove, F. D., W. B. Hanson, and F. S. Johnson (1965), Eddy Diffusion and Oxygen Transport in the Lower Thermosphere, *J. Geophys. Res.*, 70, pp. 4931–4941, doi:10.1029/JZ070i019p04931.
- [5] Colegrove, F. D., F. S. Johnson, and W. B. Hanson (1966), Atmospheric Composition in the Lower Thermosphere, *J. Geophys. Res.*, 71, pp. 2227–2236, doi:10.1029/JZ071i009p02227.
- [6] Cook, G. E. (1967), The large semi-annual variation in exospheric density: A possible explanation, *Planet. Space Sci.*, 15, pp. 627–632, doi:10.1016/0032-0633(67)90036-0.
- [7] Dickinson, R. E. and E. C. Ridley (1972), Numerical Solution for the Composition of a Thermosphere in the Presence of a Steady Subsolar-to-Antisolar Circulation with Application to Venus., *J. Atmos. Sci.*, 29, pp. 1557–1570, doi:10.1175/1520-0469(1972)029<1557:NSFTCO>2.0.CO;2.
- [8] Dickinson, R. E., E. C. Ridley, and R. G. Roble (1981), A three-dimensional general circulation model of the thermosphere, *J. Geophys. Res.*, 86, pp. 1499–1512, doi:10.1029/JA086iA03p01499.
- [9] Dickinson, R. E., E. C. Ridley, and R. G. Roble (1984), Thermospheric general circulation with coupled dynamics and composition, *J. Atmos. Sci.*, 41, pp. 205–219, doi:10.1175/1520-0469(1984)041<0205:TGCWCD>2.0.CO;2.
- [10] Forbes, J. M. (2007), Dynamics of the thermosphere, *Journal of the Meteorological Society of Japan*, 85, pp. 193–213, doi:10.2151/jmsj.85B.193.
- [11] Hagan, M. E., R. G. Roble, and J. Hackney (2001), Migrating thermospheric tides, *J. Geophys. Res.*, 106(A7), pp. 12,739–12,752, doi:10.1029/2000JA000344.
- [12] Hays, P. B., R. A. Jones, and M. H. Rees (1973), Auroral heating and the composition of the neutral atmosphere, *Planet. Space Sci.*, 21, pp. 559–573, doi:10.1016/0032-0633(73)90070-6.
- [13] Hedin, A. E. (1987), MSIS-86 thermospheric model, *J. Geophys. Res.*, 92, pp. 4649–4662, doi:10.1029/JA092iA05p04649.
- [14] Hedin, A. E. (1991), Extension of the MSIS thermosphere model into the middle and lower atmosphere, *J. Geophys. Res.*, 96, pp. 1159–1172, doi:10.1029/90JA02125.

- [15] Hedin, A. E. and G. R. Carignan (1985), Morphology of thermospheric composition variations in the quiet polar thermosphere from Dynamics Explorer measurements, *J. Geophys. Res.*, **90**, pp. 5269–5277, doi:10.1029/JA090iA06p05269.
- [16] Hedin, A. E., H. G. Mayr, C. A. Reber, N. W. Spencer, and G. R. Carignan (1974), Empirical model of global thermospheric temperature and composition based on data from the Ogo 6 quadrupole mass spectrometer, *J. Geophys. Res.*, **79**, p. 215, doi:10.1029/JA079i001p00215.
- [17] Hedin, A. E., C. A. Reber, N. W. Spencer, H. C. Brinton, and D. C. Kayser (1979), Global model of longitude/UT variations in thermospheric composition and temperature based on mass spectrometer data, *J. Geophys. Res.*, **84**, pp. 1–9, doi:10.1029/JA084iA01p00001.
- [18] Heelis, R. A., J. K. Lowell, and R. W. Spiro (1982), A model of the high-latitude ionospheric convection pattern, *J. Geophys. Res.*, **87**, 6339–6345, doi:10.1029/JA087iA08p06339.
- [19] Hodges, R. R., Jr. (1970), Vertical transport of minor constituents in the lower thermosphere by nonlinear processes of gravity waves, *J. Geophys. Res.*, **75**, pp. 4842–4848, doi:10.1029/JA075i025p04842.
- [20] Hodges, R. R., Jr. (1973), Differential equation of exospheric lateral transport and its application to terrestrial hydrogen, *J. Geophys. Res.*, **78**, pp. 7340–7346, doi:10.1029/JA078i031p07340.
- [21] Hodges, R. R., Jr., and F. S. Johnson (1968), Lateral transport in planetary exospheres, *J. Geophys. Res.*, **73**, p. 7307, doi:10.1029/JA073i023p07307.
- [22] Jacchia, L. G. (1970), New Static Models of the Thermosphere and Exosphere with Empirical Temperature Profiles, *SAO Special Report*, 313.
- [23] Johnson, F. S. and B. Gottlieb (1970), Eddy mixing and circulation at ionospheric levels, *Planet. Space Sci.*, **18**, pp. 1707–1718, doi:10.1016/0032-0633(70)90004-8.
- [24] Kasahara, A. (1974), Various Vertical Coordinate Systems Used for Numerical Weather Prediction, *Monthly Weather Review*, **102**, p. 509, doi:10.1175/1520-0493(1974)102<0509:VVCSUF>2.0.CO;2.
- [25] Kasprzak, W. T. (1969), Evidence for a helium flux in the lower thermosphere, *J. Geophys. Res.*, **74**, pp. 894–896, doi:10.1029/JA074i003p00894.
- [26] Keating, G. M. and E. J. Prior (1968), The winter helium bulge, in *Space Research VIII*, edited by A. P. Mitra, L. G. Jacchia, and W. S. Newman, p. 982.
- [27] Keating, G. M., J. A. Mullins, and E. J. Prior (1970), The polar exosphere near solar maximum., in *Space Research X*, edited by T. M. Donahue, P. A. Smith, and L. Thomas, pp. 439–449.
- [28] Keating, G. M., E. J. Prior, D. S. McDougal, and J. I. Nicholson (1974), Critical evaluation of the OGO 6 helium model, in *Space Research XV*, edited by M. J. Rycroft, pp. 273–278.

- [29] Keeling, R. F., S. C. Piper, A. F. Bollenbacher, and J. S. Walker (2009), Atmospheric CO₂ records from sites in the sio air sampling network, *Trends: A Compendium of Data on Global Change. Carbon Dioxide Information Analysis Center, Oak Ridge National Laboratory, U.S. Department of Energy, Oak Ridge, TN*, doi:10.3334/CDIAC/atg.035.
- [30] Kockarts, G. (1972), Distribution of hydrogen and helium in the upper atmosphere., *J. Atmos. Terr. Phys.*, **34**, pp. 1729–1743, doi:10.1016/0021-9169(72)90032-3.
- [31] Kockarts, G. (1973), Helium in the Terrestrial Atmosphere, *Space Science Reviews*, **14**, pp. 723–757, doi:10.1007/BF00224775.
- [32] Lei, J., T. Matsuo, X. Dou, E. K. Sutton, and X. Luan (2012), Annual and semiannual variations of thermospheric density: EOF analysis of CHAMP and GRACE data, *J. Geophys. Res.*, **117**(A16), A01310, doi:10.1029/2011JA017324.
- [33] Lettau, H. (1951), Diffusion in the upper atmosphere, in *Compendium of Meteorology*, pp. 320–333, Amer. Meteor. Soc.
- [34] Liu, X., J. P. Thayer, A. Burns, W. Wang, and E. K. Sutton (2014), Altitude variations in the thermosphere mass density response to geomagnetic activity during the recent solar minimum, *J. Geophys. Res.*, **119**, pp. 2160–2177, doi:10.1002/2013JA019453.
- [35] Liu, X., W. Wang, J. P. Thayer, A. Burns, E. K. Sutton, S. C. Solomon, L. Qian, and G. Lucas (2014), The winter helium bulge revisited, *Geophys. Res. Lett.*, **41**(19) doi:10.1002/2014GL061471.
- [36] Marcos, F. A. and J. O. Wise (2002), Towards a golden age of satellite drag, in *proceedings of the 40th AIAA Aerospace Sciences Meeting and Exhibit*, AIAA-2002-92, Reno, NV.
- [37] Marcos, F. A., M. J. Kendra, J. M. Griffin, J. N. Bass, D. R. Larson, and J. J. Liu (1998), Precision low earth orbit determination using atmospheric density calibration, *Journal of the astronautical sciences*, **46**(4), pp. 395–409.
- [38] Matsuo, T. and J. M. Forbes (2010), Principal modes of thermospheric density variability: Empirical orthogonal function analysis of CHAMP 2001-2008 data, *J. Geophys. Res.*, **115**(A14), A07309, doi:10.1029/2009JA015109.
- [39] Matsuo, T., M. Fedrizzi, T. J. Fuller-Rowell, and M. V. Codrescu (2012), Data assimilation of thermospheric mass density, *Space Weather*, **10**, S05002, doi:10.1029/2012SW000773.
- [40] Mauersberger, K., D. C. Kayser, W. E. Potter, and A. O. Nier (1976), Seasonal variation of neutral thermospheric constituents in the Northern Hemisphere, *J. Geophys. Res.*, **81**, pp. 7–11, doi:10.1029/JA081i001p00007.
- [41] Mauersberger, K., W. E. Potter, and D. C. Kayser (1976), A direct measurement of the winter helium bulge, *Geophys. Res. Lett.*, **3**, pp. 269–271, doi:10.1029/GL003i005p00269.
- [42] Mayr, H. G. and H. Volland (1972), Theoretical model for the latitude dependence of the thermospheric annual and semiannual variations, *J. Geophys. Res.*, **77**, p. 6774, doi:10.1029/JA077i034p06774.

- [43] Mayr, H. G. and H. Volland (1973), A two-component model of the diurnal variations in the thermospheric composition, *Journal of Atmospheric and Terrestrial Physics*, 35, p. 669, doi:10.1016/0021-9169(73)90198-0.
- [44] Mayr, H. G., A. E. Hedin, C. A. Reber, and G. R. Carignan (1974), Global characteristics in the diurnal variations of the thermospheric temperature and composition, *J. Geophys. Res.*, 79, p. 619, doi:10.1029/JA079i004p00619.
- [45] Mayr, H. G., I. Harris, and N. W. Spencer (1978), Some properties of upper atmosphere dynamics, *Reviews of Geophysics and Space Physics*, 16, pp. 539–565, doi:10.1029/RG016i004p00539.
- [46] Newton, G. P., D. T. Pelz, and W. T. Kasprzak (1973), Equatorial thermospheric composition and its variations, in *Space Research XIII*, edited by M. J. Rycroft and S. K. Runcorn, pp. 287–290.
- [47] Nicolet, M. (1961), Helium, an Important Constituent in the Lower Exosphere, *J. Geophys. Res.*, 66, pp. 2263–2264, doi:10.1029/JZ066i007p02263.
- [48] Picone, J. M., A. E. Hedin, D. P. Drob, and A. C. Aikin (2002), NRLMSISE-00 empirical model of the atmosphere: Statistical comparisons and scientific issues, *J. Geophys. Res.*, 107, p. 1468, doi:10.1029/2002JA009430.
- [49] Preisendorfer, R. W. (1988), *Principal component analysis in meteorology and oceanography*, Elsevier Science Ltd.
- [50] Qian, L., S. C. Solomon, and T. J. Kane (2009), Seasonal variation of thermospheric density and composition, *J. Geophys. Res.*, 114(A13), A01312, doi:10.1029/2008JA013643.
- [51] Qian, L., A. G. Burns, S. C. Solomon, and W. Wang (2013), Annual/semiannual variation of the ionosphere, *Geophys. Res. Lett.*, 40, pp. 1928–1933, doi:10.1002/grl.50448.
- [52] Reber, C. A. (1976), Dynamical effects in the distribution of helium in the thermosphere, *J. Atmos. Terr. Phys.*, 38, pp. 829–840, doi:10.1016/0021-9169(76)90023-4.
- [53] Reber, C. A., and P. B. Hays (1973), Thermospheric wind effects on the distribution of helium and argon in the Earth's upper atmosphere, *J. Geophys. Res.*, 78, p. 2977, doi:10.1029/JA078i016p02977.
- [54] Reber, C. A. and M. Nicolet (1965), Investigation of the major constituents of the April-May 1963 heterosphere by the Explorer XVII satellite, *Planet. Space Sci.*, 13, pp. 617–646, doi:10.1016/0032-0633(65)90043-7.
- [55] Reber, C. A., D. N. Harpold, R. Horowitz, and A. E. Hedin (1971), Horizontal distribution of helium in the Earth's upper atmosphere, *J. Geophys. Res.*, 76, p. 1845, doi:10.1029/JA076i007p01845.
- [56] Reber, C. A., A. E. Hedin, and S. Chandra (1973), Equatorial phenomena in neutral thermospheric composition, *J. Atmos. Terr. Phys.*, 35, p. 1223, doi:10.1016/0021-9169(73)90019-6.

- [57] Reber, C. A., A. E. Hedin, D. T. Pelz, L. H. Brace, and W. E. Potter (1975), Phase and amplitude relationships of wave structure observed in the lower thermosphere, *J. Geophys. Res.*, **80**, pp. 4576–4580, doi:10.1029/JA080i034p04576.
- [58] Richards, P. G., J. A. Fennelly, and D. G. Torr (1994), EUVAC: A solar EUV flux model for aeronomic calculations, *J. Geophys. Res.*, **99**, pp. 8981–8992, doi:10.1029/94JA00518.
- [59] Richmond, A. D., E. C. Ridley, and R. G. Roble (1992), A thermosphere/ionosphere general circulation model with coupled electrodynamics, *Geophys. Res. Lett.*, **19**, pp. 601–604, doi:10.1029/92GL00401.
- [60] Rishbeth, H. and I. C. F. M^uller-Wodarg (1999), Vertical circulation and thermospheric composition: a modelling study, *Annales Geophysicae*, **17**, pp. 794–805, doi:10.1007/s00585-999-0794-x.
- [61] Roble, R. G. and E. C. Ridley (1987), An auroral model for the NCAR thermospheric general circulation model (TGCM), *Annales Geophysicae*, **5**, 369–382.
- [62] Roble, R. G., and E. C. Ridley (1994), A thermosphere-ionosphere-mesosphere-electrodynamics general circulation model (time-GCM): Equinox solar cycle minimum simulations (30-500 km), *Geophys. Res. Lett.*, **21**, pp. 417–420, doi:10.1029/93GL03391.
- [63] Roble, R. G., E. C. Ridley, A. D. Richmond, and R. E. Dickinson (1988), A coupled thermosphere/ionosphere general circulation model, *Geophys. Res. Lett.*, **15**, pp. 1325–1328, doi:10.1029/GL015i012p01325.
- [64] Schunk, R. W. and A. F. Nagy (2004), *Ionospheres*, Cambridge Atmospheric and Space Science Series.
- [65] Seidelmann, P. K. (1992), *Explanatory Supplement to the Astronomical Almanac*, University Science Books.
- [66] Solomon, S. C. and L. Qian (2005), Solar extreme-ultraviolet irradiance for general circulation models, *J. Geophys. Res.*, **110**(A9), A10306, doi:10.1029/2005JA011160.
- [67] Solomon, S. C., L. Qian, L. V. Didkovsky, R. A. Viereck, and T. N. Woods (2011), Causes of low thermospheric density during the 2007-2009 solar minimum, *J. Geophys. Res.*, **116**, A00H07, doi:10.1029/2011JA016508.
- [68] Solomon, S. C., A. G. Burns, B. A. Emery, M. G. Mlynczak, L. Qian, W. Wang, D. R. Weimer, and M. Wiltberger (2012), Modeling studies of the impact of high-speed streams and co-rotating interaction regions on the thermosphere-ionosphere, *J. Geophys. Res.*, **117**, A00L11, doi:10.1029/2011JA017417.
- [69] Storz, M. F., B. R. Bowman, M. J. I. Branson, S. J. Casali, and W. K. Tobiska (2005), High accuracy satellite drag model (HASDM), *Advances in Space Research*, **36**, pp. 2497–2505, doi:10.1016/j.asr.2004.02.020.
- [70] Sutton, E. K. (2011), Accelerometer-derived atmospheric density from the CHAMP and GRACE satellites, *AFRL Tech. Memorandum*, DTIC# ADA537198.

- [71] Sutton, E. K., S. B. Cable, C. S. Lin, L. Qian, and D. R. Weimer (2012), Thermospheric basis functions for improved dynamic calibration of semi-empirical models, *Space Weather*, 10(10), S10001, doi:10.1029/2012SW000827.
- [72] Sutton, E. K., J. P. Thayer, W. Wang, S. C. Solomon, X. Liu, and B. T. Foster (2015), A self-consistent model of helium in the thermosphere, *Journal of Geophysical Research: Space Physics*, doi:10.1002/2015JA021223.
- [73] Swarztrauber, P. (1979), On the spectral approximation of discrete scalar and vector functions on the sphere, *SIAM Journal on Numerical Analysis*, 16(6), pp. 934–949, doi:10.1137/0716069.
- [74] Thayer, J. P., X. Liu, J. Lei, M. Pilinski, and A. G. Burns (2012), The impact of helium on thermosphere mass density response to geomagnetic activity during the recent solar minimum, *Journal of Geophysical Research (Space Physics)*, 117, A07315, doi:10.1029/2012JA017832.
- [75] Viereck, R. A., L. E. Floyd, P. C. Crane, T. N. Woods, B. G. Knapp, G. Rottman, M. Weber, L. C. Puga, and M. T. Deland (2004), A composite Mg II index spanning from 1978 to 2003, *Space Weather*, 2, p. 10005, doi:10.1029/2004SW000084.
- [76] Weimer, D. R. (2005), Improved ionospheric electrodynamic models and application to calculating Joule heating rates, *J. Geophys. Res.*, 110(A9), A05306, doi:10.1029/2004JA010884.
- [77] Woods, T. N. and G. J. Rottman (2002), Solar Ultraviolet Variability Over Time Periods of Aeronomic Interest, *Washington DC American Geophysical Union Geophysical Monograph Series*, 130, p. 221.
- [78] Zhang, Y. and L. J. Paxton (2008), An empirical Kp-dependent global auroral model based on TIMED/GUVI FUV data, *J. Atmos. Sol.-Terr. Phys.*, 70, pp. 1231–1242, doi:10.1016/j.jastp.2008.03.008.

Appendix A: In-House Activities

List of Tables

A-1 Funding Summary by Cost Category 44
A-2 Personnel 44

A.1 Final Laboratory Task Report

LRIR #: 13RV09COR

Reporting Period: Fiscal Year 2013–2015

Laboratory Task Manager: Eric Sutton

Commercial Phone: (505) 846-7846 **DSN:** 246-7846

Mailing Address:

RVBXI / Bldg. 570 / Rm. 2363
3550 Aberdeen Ave SE
Kirtland AFB, NM 87117

E-Mail Address: eric.sutton.5@us.af.mil

AFOSR Program Manager: Kent Miller

Table A-1: Funding Summary by Cost Category

Year	In-House	Capital Equip. (>\$ 5K each)	Non-Capital Equip. (<\$ 5K each)	Travel	On-Site Contractor	Total
FY13	138K	—	—	3K	9K	150K
FY14	142K	—	3K	5K	—	150K
FY15	144K	—	—	6K	—	150K

Table A-2: Personnel

Name	Degree	Discipline	Involvement
Air Force Employees:			
Eric Sutton	PhD	Physicist	0.38 Man-Yr/Yr
Samuel Cable	PhD	Physicist	0.10 Man-Yr/Yr

A.2 Invited Talks and Lectures

Sutton, E. K. (2015), Dynamical influences on thermospheric composition (invited), AGU Fall Meeting, Dec. 2015 (tentatively scheduled).

Sutton, E. K., and F. Schmidt (2015), First Principle Modeling of the Upper Thermosphere/Lower Exosphere (invited), CEDAR Workshop, Seattle, WA, 21–25 June, 2015.

- Sutton, E. K.** (2015), Satellite Accelerometer Observations During the Storms and Substorms Without Borders Campaigns (invited), CEDAR Workshop, Seattle, WA, 21–25 June, 2015.
- Sutton, E. K.** (2015), The Upper Atmosphere and its Influence on Satellite Motion (invited Lecture), University of New Mexico, ECE graduate course on Space Weather, Albuquerque, NM, 27 April, 2015.
- Sutton, E. K.** (2013), The Role of Helium in the Thermosphere During Recent Solar Minima, Invited Guest Lecturer, HAO Colloquium Series, NCAR/HAO, Boulder, CO, 8 August 2013.
- Sutton, E. K.** (2011), Upper Atmosphere Modeling at AFRL, Invited Speaker, 1st IMPACT Team Meeting, LANL, Santa Fe, NM, 19 October, 2011.

A.3 Scientific Visits

- Sutton, E. K.** (2015), NCAR/HAO Visiting Scientist Program, Boulder, CO, 19-21 January 2015.
- Sutton, E. K.** (2013), NCAR/HAO Visiting Scientist Program, Boulder, CO, 5-9 August 2013.

A.4 Publications

A.4.1 First-Authored

- Sutton, E. K.**, J. P. Thayer, W. Wang, S. C. Solomon, X. Liu, and B. T. Foster (2015), A self-consistent model of helium in the thermosphere, *Journal of Geophysical Research: Space Physics*, pp. n/a–n/a, doi:10.1002/2015JA021223.
- Sutton, E. K.**, **S. B. Cable**, C. S. Lin, L. Qian, and D. R. Weimer (2012), Thermospheric basis functions for improved dynamic calibration of semi-empirical models, *Space Weather*, 10, S10001, doi:10.1029/2012SW000827.

A.4.2 Co-Authored

- Huang, C. Y., Y. Huang, Y.-J. Su, **E. K. Sutton**, **E. K.**, M. Hairston, and W. R. Coley (2015, accepted), Ionosphere-Thermosphere Response to Solar Wind Forcing During Magnetic Storms, accepted for publication in the *J. Space Wea. Space Clim.*
- Yamazaki, Y., M. J. Kosch, and **E. K. Sutton** (2015), North-south asymmetry of the high-latitude thermospheric density: IMF BY effect, *Geophys. Res. Lett.*, 42, 225–232, doi:10.1002/2014GL062748.
- Liu, X., W. Wang, J. P. Thayer, A. Burns, **E. K. Sutton**, S. C. Solomon, L. Qian, and G. Lucas (2014), The winter helium bulge revisited, *Geophys. Res. Lett.*, 41, 6603–6609, doi:10.1002/2014GL061471.
- Vickers, H., M. J. Kosch, **E. K. Sutton**, L. Bjoland, Y. Ogawa, and C. La Hoz (2014), A solar cycle of upper thermosphere density observations from the EISCAT Svalbard Radar, *J. Geophys. Res. (Space Physics)*, 119, 6833–6845, doi:10.1002/2014JA019885.
- Liu, X., J. P. Thayer, A. Burns, W. Wang, and **E. K. Sutton** (2014), Altitude variations in the thermosphere mass density response to geomagnetic activity during the recent solar minimum, *J. Geophys. Res. (Space Physics)*, 119, 2160–2177, doi:10.1002/2013JA019453.

- Huang, C. Y., Y.-J. Su, **E. K. Sutton**, D. R. Weimer, and R. L. Davidson (2014), Energy coupling during the August 2011 magnetic storm, *J. Geophys. Res. (Space Physics)*, 119, 1219–1232, doi:10.1002/2013JA019297.
- Mehta, P. M., C. A. McLaughlin, and **E. K. Sutton** (2013), Drag Coefficient Modeling for GRACE using Direct Simulation Monte Carlo, *Adv. Space Res.*, 52 (12), doi:10.1016/j.asr.2013.08.033.
- Huang, C. Y., P. A. Roddy, **E. K. Sutton**, R. Stoneback, R. F. Pfaff, L. C. Gentile, S. H. Delay (2013), Ion-neutral coupling during deep solar minimum, *J. Atmos. Sol.-Terr. Phys.*, 103, doi:10.1016/j.jastp.2012.11.009.
- Vickers, H., M. J. Kosch, **E. K. Sutton**, Y. Ogawa, and C. La Hoz (2013), Thermospheric atomic oxygen density estimates using the EISCAT Svalbard Radar, *J. Geophys. Res. (Space Physics)*, 118, 1319–1330, doi:10.1002/jgra.50169.
- Titov, E. V., J. M. Burt, E. Josyula, **E. K. Sutton**, and C. S. Lin (2013), Uncertainties in Satellite Drag Associated with Variations in Atmospheric Conditions, in proc. 5th AIAA Atmospheric and Space Environments Conference, San Diego, CA, 24-27 June 2013, AIAA 2013-2683, doi:10.2514/6.2013-2683.
- Mishin, E., E. Sutton, G. Milikh, I. Galkin, C. Roth, and M. Frster (2012), F2-region atmospheric gravity waves due to high-power HF heating and subauroral polarization streams, *Geophys. Res. Lett.*, 39, L11101, doi:10.1029/2012GL052004.
- Lei, J., T. Matsuo, X. Dou, **E. K. Sutton**, and X. Luan (2012), Annual and semiannual variations of thermospheric density: EOF analysis of CHAMP and GRACE data, *J. Geophys. Res.*, 117, A01310, doi:10.1029/2011JA017324.
- Shim, J. S., . . . , **E. K. Sutton**, et al. (2012), CEDAR Electrodynamics Thermosphere Ionosphere (ETI) Challenge for Systematic Assessment of Ionosphere/Thermosphere Models 2: Electron density, Neutral density, NmF2, and hmF2 Using Space Based Observations, *Space Weather*, doi:10.1029/2012SW000851.
- Lei, J., A. G. Burns, J. P. Thayer, W. Wang, M. G. Mlynczak, L. A. Hunt, X. Dou, and **E. K. Sutton** (2012), Overcooling in the upper thermosphere during the recovery phase of the 2003 October storms, *J. Geophys. Res.*, 117, A03314, doi:10.1029/2011JA016994.
- Huang, C. Y., S. H. Delay, P. A. Roddy, **E. K. Sutton**, and R. Stoneback (2012), Longitudinal structures in the equatorial ionosphere during deep solar minimum, *J. Atmos. Sol.-Terr. Phys.*, 90-91, doi:10.1016/j.jastp.2012.04.012.
- Wise, J. O., W. J. Burke, and **E. K. Sutton** (2012), Globally averaged exospheric temperatures derived from CHAMP and GRACE accelerometer measurements, *J. Geophys. Res.*, 117, A04312, doi:10.1029/2011JA017108.

A.5 Presentations

- Sutton, E. K.**, and F. Schmidt, First Principle Modeling of the Upper Thermosphere/Lower Exosphere (invited), CEDAR Workshop, Seattle, WA, 21–25 June, 2015.
- Sutton, E. K.** (2015), Satellite Accelerometer Observations During the Storms and Substorms Without Borders Campaigns (invited), CEDAR Workshop, Seattle, WA, 21–25 June, 2015.
- Thayer, J. P., X. Liu, W. Wang, A. Burns, **E. K. Sutton**, Composition change and its effect on thermosphere mass density response during geomagnetic activity, European Geophysical Union Gen. Assemb., Vienna, Austria, 27 April – 2 May, 2014.

- Koller, J., . . . , **E. K. Sutton**, et al., IMPACT: Integrated Modeling of Perturbations in Atmospheres for Conjunction Tracking, AGU Fall Meeting, abstract #SM52C-08, Dec. 2013.
- Huang, C. Y.; Y. Su, **E. K. Sutton**, D. R. Weimer, R. Davidson, Energy coupling during the August 2011 magnetic storm, AGU Fall Meeting, abstract #SM41A-2215, Dec. 2013.
- Weimer, D. R., T. Edwards, **E. K. Sutton**, and E. Doornbos, Storm-time and quiescent variations in the thermosphere exhibited in maps of exospheric temperatures, AGU Fall Meeting, abstract #SA33C-06, Dec. 2013.
- Liu, X., J. P. Thayer, W. Wang, A. G. Burns, and **E. K. Sutton**, Composition change and its effect on mass density response during geomagnetic storm, AGU Fall Meeting, abstract #SA33C-03, Dec. 2013.
- Shi, Y., E. Zesta, H. K. Connor, Y. Su, **E. K. Sutton**, C. Y. Huang, D. Ober, C. Christodoulou, High-latitude Thermosphere Response to Solar Wind Dynamic Pressure Enhancements, AGU Fall Meeting, abstract #SA31A-1968, Dec. 2013.
- Shi, Y., E. Zesta, **E. K. Sutton**, J. O. Wise, Y. Su, S. H. Delay, Effect of Solar Wind Dynamic Pressure Enhancements on Thermosphere Density, AGU Fall Meeting, abstract #SA33A-2172, Dec. 2012.
- Vickers, H., M. J. Kosch, **E. K. Sutton**, Y. Ogawa, C. La Hoz, Thermospheric atomic oxygen density estimates using the EISCAT Svalbard Radar, AGU Fall Meeting, abstract #SA31A-2143, Dec. 2012.
- Huang, C. Y., Y. Su, **E. K. Sutton**, D. R. Weimer, G. D. Earle, A. J. Gerrard, D. M. Ober, G. R. Wilson, R. Davidson, Ion-neutral Coupling During the August 2011 Magnetic Storm. AGU Fall Meeting, abstract #SA31A-2137, Dec. 2012.
- Emery, B. A., . . . , **E. K. Sutton**, et al., Climatology Assessment of Ionosphere/Thermosphere Models in Low Solar Flux Conditions for the CCMC CEDAR Challenge, AGU Fall Meeting, abstract #SA23A-2152, Dec. 2012.
- Sutton, E. K.**, C. S. Lin, and **S. B. Cable**, Comparison of TIE-GCM SigmaO/N2 Column Ratios with Measurements of the SSUSI Instrument, AGU Fall Meeting, abstract #SA23A-2151, Dec. 2012.
- Cable, S. B.**, **E. K. Sutton**, T. Matsuo, and C. S. Lin, Model bias characteristics for data assimilation in the thermosphere, AGU Fall Meeting, abstract #SA21A-1869, Dec. 2011.
- Lin, C. S.; Knipp, D.; Marcos, F.; **Cable, S. B.**; **Sutton, E. K.**, Survey of Thermosphere Joule Heating Locations and Magnetic Disturbance Conditions, AGU Fall Meeting, abstract #SA41A-1824, Dec. 2011.
- Huang, C. Y., S. H. Delay, P. A. Roddy, **E. K. Sutton**, R. Stoneback, and R. F. Pfaff, Ionosphere-thermosphere coupling during deep solar minimum, AGU Fall Meeting, abstract #SA21B-04, Dec. 2011.
- Shim, J., . . . , **E. K. Sutton**, et al., Systematic Assessment of Ionosphere/Thermosphere Models during the 2006 AGU Storm, AGU Fall Meeting, abstract #SA41B-1857, Dec. 2011.
- Sutton, E. K.**, **S. B. Cable**, F. A. Marcos, and C. S. Lin, Improved basis functions for dynamic calibration of semi-empirical thermospheric models, AGU Fall Meeting, abstract #SM31B-2096, Dec. 2011.
- Wise, J. O., **E. K. Sutton**, F. A. Marcos, and W. J. Burke, Modeled Composition of the Thermosphere at Solar Minimum using CHAMP and GRACE, AGU Fall Meeting, abstract #SA11B-1593, Dec. 2011.

A.6 Professional Activities

Journal reviews: GRL, JGR, Space Weather, ASR, AIAA, AAS

Proposal reviews: NSF, AFRL, AFOSR, SBIR/STTR

Student mentoring: Lt. Frederick Schmidt, AFIT, masters thesis defense: Feb. 2016; Mr. Justin Bock, U. Minnesota/AFRL Space Scholar, 2014; Regular interactions with NRC postdocs at AFRL

A.7 Technology assists, transitions, or transfers

Table A-1: Technology assists, transitions, or transfers

Task Title	PoP	AFOSR Program Manager	Performer	Customer	Research Result	Application	Form	To
TIE-GCM-He model transition to 6.2 and FFRDC	FY13–FY15	Kent Miller	Eric Sutton	(1) Eric Sutton PI for ODE and DTIC-LEO (2) Stan Solomon, NCAR Senior Scientist, stans@ucar.edu	Produced new model of the atmosphere accurately specifies the vertical structure of the upper thermosphere.	Pd: Model will aid in future operationalization of hybrid model and physics-based model for satellite drag applications	L	(1) AF (2) G-FFRDC
Accelerometer-derived density	FY13–FY15	Kent Miller	Eric Sutton	(1) Bruce Bowman, AFSPC (2) Mariangel Fedrizzi, NOAA (3) Josef Koller, LANL (4) Liying Qian, NCAR (5) Various academic collaborators	Extension of existing accelerometer density dataset Test and Validation of high-altitude (800 km) satellite drag data with accelerometer data (450 km).	Pd: Used for scientific studies and satellite drag research	L	(1) AF (2) O-govt (3) O-FFRDC (4) O-FFRDC (5) O-univ.
J70/TIE-GCM hybrid delivery	FY13–FY15	Kent Miller	Eric Sutton	Chin Lin, ODE Program, chin.lin@kirtland.af.mil, (505) 846-7803	Produced hybrid model of the thermosphere a mix between empirical models and physics-based models.	Pd: The hybrid model will be tested and validated at the 6.2 level.	L	AF

Note: In each of the last three columns, enter the appropriate codes from the lists below:

Transitioned To:

Industry = I; Air Force 6.2 or 6.3 = AF;
Other AF, DoD, Government, etc. = O
(please specify)

Application:

Product (New or Improved) = Pd;
Process (New or Improved) = Pc;
Other = O (please specify)

Transitioned From:

AFRL = L; Industry = I; Academia = A

Appendix B: Time-dependent thermospheric composition for N components

B.1 Introduction and Nomenclature

In this section, an equation describing the evolution of major species composition in a log-pressure coordinate frame is derived by combining the species-dependent continuity and diffusion equations. The derivation closely follows that of *Dickinson and Ridley* [7]; however, additional terms describing time dependence, eddy and thermal diffusion are included to reflect the current implementation within the TIE-GCM. We also deviate slightly from their treatment to highlight several equations that are useful in tracking species-dependent as well as mass-averaged transport. The following definitions are used:

D_{ij}	mutual diffusion coefficient of i th and j th components
g	gravitational acceleration
H_i	scale height of i th component $[= kT/(m_i g)]$
H	scale height of mixture $[= kT/(\bar{m} g)]$
\hat{K}_E, K_E	eddy diffusion coefficients
k	Boltzmann constant
\mathbf{L}	differential matrix operator of normalized pressure forces
m_i	molecular mass of i th component
\bar{m}	mean molecular mass $[= (\sum_{i=1}^N n_i m_i)/n]$
n_i	number density of i th component
n	total number density $[= \sum_{i=1}^N n_i]$
p_i	partial pressure of i th component $[= n_i kT]$
p_0	reference pressure
p	pressure
S_i	source or sink for number density of i th component
\mathbf{s}	vector containing the first $(N-1)$ components of $m_i S_i / \rho$
T	temperature
\mathbf{V}	horizontal component of the momentum-weighted mean velocity
\hat{w}	vertical component of the momentum-weighted mean velocity $[= D\hat{z}/Dt]$
w_i	deviation of vertical velocity of i th component from mean velocity
w'_i	contribution to w_i from molecular diffusion
w''_i	contribution to w_i from eddy diffusion
\mathbf{w}	vector containing the first $(N-1)$ components of $n_i m_i w_i$
\mathbf{w}'	vector containing the first $(N-1)$ components of $n_i m_i w'_i$
\mathbf{w}''	vector containing the first $(N-1)$ components of $n_i m_i w''_i$
\hat{z}	vertical spatial coordinate
z	vertical log-pressure coordinate $[= \ln(p_0/p)]$
α	diffusion matrix
α_{Ti}	thermal diffusion coefficient of i th component
θ	latitude
λ	longitude

- ν_i volume mixing ratio of i th component [= n_i/n]
- ρ mass density of mixture [= $\sum_{i=1}^N n_i m_i$]
- ψ_i relative density of i th component [= $n_i m_i / \rho$]
- Ψ vector containing the first $(N-1)$ components of ψ_i
- ω vertical motion relative to log-pressure coordinates [= Dz/Dt]

B.2 Mass Continuity

Neglecting horizontal diffusion, each component satisfies the following continuity equation:

$$\frac{\partial}{\partial \hat{z}}(n_i m_i w_i) = m_i S_i - \frac{\partial}{\partial t}(n_i m_i) - \nabla \cdot (n_i m_i \mathbf{V}) - \frac{\partial}{\partial \hat{z}}(n_i m_i \hat{w}) \quad (\text{B-1})$$

The right-hand side of (B-1) can be written in terms of the relative densities:

$$\frac{\partial}{\partial \hat{z}}(n_i m_i w_i) = m_i S_i - \left(\frac{\partial}{\partial t}(\psi_i \rho) + \nabla \cdot (\psi_i \rho \mathbf{V}) + \frac{\partial}{\partial \hat{z}}(\psi_i \rho \hat{w}) \right) \quad (\text{B-2})$$

We wish to transform Eq. (B-2) from a spatial to a log-pressure vertical coordinate system under the assumption of hydrostatic equilibrium using the following relationship:

$$d\hat{z} = H dz \quad (\text{B-3})$$

When applying this transformation to partial derivatives with respect to time and horizontal spatial coordinates, the vertical coordinate being held constant must be considered. The following equations, which also require the assumption of hydrostatic equilibrium, are used to complete this transformation [[24] - Eqs. (3.6) and (3.17)]:

$$\left(\frac{\partial}{\partial t} \right)_{\hat{z}} (\psi_i \rho) = \left(\frac{\partial}{\partial t} \right)_z (\psi_i \rho) - \frac{1}{H} \left(\frac{\partial \hat{z}}{\partial t} \right)_z \frac{\partial}{\partial z} (\psi_i \rho) \quad (\text{B-4})$$

$$\nabla_{\hat{z}} \cdot (\psi_i \rho \mathbf{V}) = \nabla_z \cdot (\psi_i \rho \mathbf{V}) - \frac{1}{H} (\nabla_z \hat{z}) \cdot \frac{\partial}{\partial z} (\psi_i \rho \mathbf{V}) \quad (\text{B-5})$$

where the subscripts \hat{z} and z refer to the vertical coordinate being held constant under partial differentiation. Additionally, the relationship between the spatial and log-pressure vertical velocities is as follows [[24] - Eq. (3.12)]:

$$\hat{w} = \omega H + \left(\frac{\partial \hat{z}}{\partial t} \right)_z + \mathbf{V} \cdot \nabla_z \hat{z} \quad (\text{B-6})$$

Making the appropriate substitutions, noting that the equation of state and our assumption of hydrostatic equilibrium imply:

$$\rho H = \frac{p_0}{g} e^{-z} \quad (\text{B-7})$$

and dropping the subscript ' z ' from derivatives taken with respect to time and horizontal spatial coordinates, Eq. (B-2) becomes:

$$\frac{\partial}{\partial z}(n_i m_i w_i) = -\frac{p_0 e^{-z}}{g} \left(\frac{\partial \psi_i}{\partial t} + \nabla \cdot (\psi_i \mathbf{V}) + e^z \frac{\partial}{\partial z}(\psi_i e^{-z} \omega) - \frac{m_i S_i}{\rho} \right) \quad (\text{B-8})$$

The definition of w_i implies:

$$\sum_{i=1}^N n_i m_i w_i = 0 \quad (\text{B-9})$$

Mass sources are assumed to arise solely from the dissociation of one molecule into others so that:

$$\sum_{i=1}^N m_i S_i = 0 \quad (\text{B-10})$$

Relative densities ψ_i are defined so that:

$$\sum_{i=1}^N \psi_i = 1 \quad (\text{B-11})$$

By combining (B-8) for each component and noting (B-9), (B-10), and (B-11), the continuity equation describing the total fluid in log-pressure coordinates is obtained:

$$\nabla \cdot \mathbf{V} + e^z \frac{\partial}{\partial z}(e^{-z} \omega) = 0 \quad (\text{B-12})$$

Thus, by invoking the assumption of hydrostatic equilibrium and adopting pressure coordinates, the mass flow of the fluid appears incompressible, transforming the mass continuity equation from a prognostic to a diagnostic equation (i.e. no time derivatives appear in the equation).

Using Eq. (B-12), the divergence terms of Eq. (B-8) can be simplified in favor of advection terms, yielding the following equation:

$$\frac{\partial}{\partial z}(n_i m_i w_i) = -\frac{p_0 e^{-z}}{g} \left(\frac{\partial \psi_i}{\partial t} + \mathbf{V} \cdot \nabla \psi_i + \omega \frac{\partial \psi_i}{\partial z} - \frac{m_i S_i}{\rho} \right) \quad (\text{B-13})$$

Now let \mathbf{w} be the $(N-1)$ vector with components $m_i n_i w_i$, \mathbf{s} the $(N-1)$ vector with components $m_i S_i / \rho$, and Ψ the $(N-1)$ vector with elements ψ_i . Then the first $(N-1)$ equations of (B-13) can be written in vector form as:

$$\frac{\partial}{\partial z} \mathbf{w} = -\frac{p_0}{g} e^{-z} \left(\frac{\partial \Psi}{\partial t} + \mathbf{V} \cdot \nabla \Psi + \omega \frac{\partial \Psi}{\partial z} - \mathbf{s} \right) \quad (\text{B-14})$$

B.3 Molecular and Thermal Diffusion

With the assumption that the atmosphere is in a state of hydrostatic equilibrium, i.e. $\partial p / \partial \hat{z} = -\rho g$, the equation of motion for the i th component of an N -component mixture in the presence of molecular and thermal diffusion [[3] - Eqs. (18.2,5) and (18.3,13)] can be written:

$$\sum_{j \neq i}^N \frac{n_i n_j}{n D_{ij}} (w'_j - w'_i) = n_i \left(\frac{1}{p_i} \frac{\partial p_i}{\partial \hat{z}} + \frac{1}{H_i} + \frac{\alpha_{T_i}}{T} \frac{\partial T}{\partial \hat{z}} \right) \quad (\text{B-15})$$

The pressure force exerted on molecules of the i th component, expressed by the right-hand side of (B-15), forces these molecules to flow through the rest of the mixture in balance with collisional drags given by the left-hand side.

Noting the partial pressure $p_i = p \psi_i = m/m_i$, (B-15) becomes:

$$\frac{1}{n} \sum_{j \neq i}^N \left[\frac{\psi_i}{m_j D_{ij}} (n_j m_j w'_j) - \frac{\psi_j}{m_j D_{ij}} (n_i m_i w'_i) \right] = \left[\frac{\partial}{\partial \hat{z}} - \left(\frac{1}{H} - \frac{1}{H_i} - \frac{1}{\bar{m}} \frac{\partial \bar{m}}{\partial \hat{z}} - \frac{\alpha_{T_i}}{T} \frac{\partial T}{\partial \hat{z}} \right) \right] \psi_i \quad (\text{B-16})$$

Eqs. (B-9) and (B-11)—noting that the former applies to ticked quantities as well—are now used to eliminate w' and ψ_N from the first $(N-1)$ equations of (B-16), giving for the i th component:

$$\sum_{j=1}^{N-1} \hat{\alpha}_{ij} (m_j n_j w'_j) = \left[\frac{\partial}{\partial \hat{z}} - \left(\frac{1}{H} - \frac{1}{H_i} - \frac{1}{\bar{m}} \frac{\partial \bar{m}}{\partial \hat{z}} - \frac{\alpha_{T_i}}{T} \frac{\partial T}{\partial \hat{z}} \right) \right] \psi_i \quad (\text{B-17})$$

where

$$\hat{\alpha}_{ij} = \begin{cases} -\frac{1}{n} \left[\frac{1}{m_N D_{iN}} + \sum_{k \neq i}^{N-1} \left(\frac{1}{m_k D_{ik}} - \frac{1}{m_N D_{iN}} \right) \psi_k \right], & j = i \\ \frac{1}{n} \left(\frac{1}{m_j D_{ij}} - \frac{1}{m_N D_{iN}} \right) \psi_i, & j \neq i \end{cases} \quad (\text{B-18})$$

and m_N refers to the molecular mass of the N th species.

Now let $\hat{\alpha}$ be the $(N-1) \times (N-1)$ matrix with elements $\hat{\alpha}_{ij}$, and \hat{L} the diagonal matrix of differential operators with elements:

$$\hat{L}_{ij} = \delta_{ij} \left[\frac{\partial}{\partial \hat{z}} - \left(\frac{1}{H} - \frac{1}{H_i} - \frac{1}{\bar{m}} \frac{\partial \bar{m}}{\partial \hat{z}} - \frac{\alpha_{T_i}}{T} \frac{\partial T}{\partial \hat{z}} \right) \right] \quad (\text{B-19})$$

The solution of the nonsingular system of Eqs. (B-17) can now be expressed in matrix form:

$$\mathbf{w}' = \hat{\alpha}^{-1} \hat{L} \Psi \quad (\text{B-20})$$

Following *Dickinson and Ridley* [7], a nondimensional form of the diffusion matrix $\hat{\alpha}$ can be derived using a nondimensional parameter ϕ_{ij} related to the mutual diffusion coefficient through:

$$\phi_{ij} = \frac{m_N D}{m_j D_{ij}} \quad (\text{B-21})$$

where D is a characteristic diffusion coefficient. It is assumed that D varies with pressure and temperature in the following way:

$$D = D_0 \left(\frac{p_{00}}{p} \right) \left(\frac{T}{T_{00}} \right)^{1.75} \quad (\text{B-22})$$

where $D_0 = 0.2$ is the characteristic diffusion coefficient at S.T.P., $T_{00} = 273$ K, $p_{00} = 10^6$ g/(cm · s²).

The parameter $\hat{\alpha}_{ij}$ defined by Eq. (B-18) is nondimensionalized by the substitution

$$\alpha_{ij} = (m_N n D) \hat{\alpha}_{ij} \quad (\text{B-23})$$

where the nondimensional parameter α_{ij} is then

$$\alpha_{ij} = \begin{cases} -\left[\phi_{iN} + \sum_{k \neq i}^{N-1} (\phi_k - \phi_{iN}) \psi_k\right], & j = i \\ (\phi_{ij} - \phi_{iN}) \psi_i, & j \neq i \end{cases} \quad (\text{B-24})$$

Additionally, Eqs. (B-3) and (B-7) are again used to transform the vertical coordinate of the right-hand-side of Eq. (B-20) into log-pressure levels, resulting in:

$$\mathbf{w}' = \tau^{-1} \left(\frac{T_{00}}{T} \right)^{0.25} \frac{p_0 \bar{m}}{m_N g} \boldsymbol{\alpha}^{-1} \mathbf{L} \boldsymbol{\Psi} \quad (\text{B-25})$$

where

$$L_{ij} = \delta_{ij} \left[\frac{\partial}{\partial z} - \left(1 - \frac{m_i}{\bar{m}} - \frac{1}{\bar{m}} \frac{\partial \bar{m}}{\partial z} - \frac{\alpha_{Ti}}{T} \frac{\partial T}{\partial z} \right) \right] \quad (\text{B-26})$$

τ is a characteristic diffusion timescale defined by:

$$\tau = \frac{p_0}{p_{00}} \frac{H_0^2}{D_0} \quad (\text{B-27})$$

and H_0 is a characteristic scale height:

$$H_0 = \frac{k T_{00}}{m_N g} \quad (\text{B-28})$$

B.4 Eddy Diffusion

In an atmosphere dominated by a single constituent, as is the case with molecular nitrogen in the lower thermosphere, eddy diffusion establishes a flow which acts to smooth gradients in the volume mixing ratio of the minor constituents, ν_i , as follows [33, 4]:

$$w_i'' = -\hat{K}_E \frac{1}{\nu_i} \frac{\partial \nu_i}{\partial \hat{z}} \quad (\text{B-29})$$

In terms of mass flow rates and mixing ratios, Eq. (B-29) becomes:

$$n_i m_i w_i'' = -n \bar{m} \hat{K}_E \left(\frac{\partial}{\partial \hat{z}} + \frac{1}{\bar{m}} \frac{\partial \bar{m}}{\partial \hat{z}} \right) \psi_i \quad (\text{B-30})$$

Transforming to log-pressure coordinates and writing in vector form, Eq. (B-30) becomes:

$$\mathbf{w}'' = -\frac{p_0}{g} K_E e^{-z} \left(\frac{\partial}{\partial z} + \frac{1}{\bar{m}} \frac{\partial \bar{m}}{\partial z} \right) \boldsymbol{\Psi} \quad (\text{B-31})$$

where $K_E \equiv \hat{K}_E / H^2$.

B.5 Composition Equation

Setting the total species-dependent mass flux $w = w' + w''$ and combining Eqs. (B-25) and (B-31) to eliminate w from Eq. (B-14) yields the composition equation:

$$\frac{\partial}{\partial z} \left[\tau^{-1} \left(\frac{T_{00}}{T} \right)^{0.25} \frac{\bar{m}}{m_N} \alpha^{-1} \mathbf{L} \Psi - K_E e^{-z} \left(\frac{\partial}{\partial z} + \frac{1}{\bar{m}} \frac{\partial \bar{m}}{\partial z} \right) \Psi \right] = e^{-z} \left(\mathbf{s} - \frac{\partial \Psi}{\partial t} - \mathbf{V} \cdot \nabla \Psi - \omega \frac{\partial}{\partial z} \Psi \right) \quad (\text{B-32})$$

In the current TIE-GCM implementation, the subscripting order of the major neutral species is as follows: $i = \{\text{O}_2, \text{O}, \text{He}\}$, with N_2 chosen to be the N th species due in part to the assumptions stated in Section B.4.

DISTRIBUTION LIST

DTIC/OCF	
8725 John J. Kingman Rd, Suite 0944	
Ft Belvoir, VA 22060-6218	1 cy
AFRL/RVIL	
Kirtland AFB, NM 87117-5776	2 cys
Official Record Copy	
AFRL/RVBXI/Dr. Eric Sutton	1 cy